Wave Motion 94 (2020) 102523

Contents lists available at ScienceDirect

Wave Motion

journal homepage: www.elsevier.com/locate/wamot

Active control of Helmholtz fields in 3D using an array of sources

Neil Jerome A. Egarguin [a,b,*], Shubin Zeng [c], Daniel Onofrei [a], Jiefu Chen [c]

[a] Department of Mathematics, University of Houston, United States of America
[b] Institute of Mathematical Sciences and Physics, University of the Philippines Los Baños, Philippines
[c] Department of Electrical and Computer Engineering, University of Houston, United States of America

ARTICLE INFO

Article history:
Received 13 August 2019
Received in revised form 26 January 2020
Accepted 27 January 2020
Available online 30 January 2020

ABSTRACT

In this paper, we present a strategy for the active manipulation of Helmholtz fields using an array (swarm) of coupling sources with prescribed fixed positions. More specifically, we consider the problem of using an array of active surface sources to approximate prescribed fields in several given exterior regions of space including possibly the far field region. In this regard, we extend the results presented in our previous works for the case of a single source to allow for multiple active sources considering the first-order mutual coupling between them. We prove the existence of boundary inputs on the sources (pressure or normal velocity), so that the desired control effect is obtained. We also devise a stable numerical scheme to compute these boundary inputs by using local basis functions defined on the source boundaries in a method of moments approach together with a Morozov discrepancy principle-based Tikhonov regularization. Several numerical simulations were presented to demonstrate the accuracy of the proposed scheme.

1. Introduction and related works

Helmholtz fields and the development of schemes to actively manipulate them have been the subject of numerous studies due to its wide range of possible applications. Common applications include active noise cancellation [1–5], sound synthesis and reproduction [6–11], and active control of acoustic scattered fields with application to cloaking and shielding [12–19]. A more comprehensive discussion and analysis of some of the methods employed in these applications are also given in [20] for scattered field control and in [21] and [22] for sound field synthesis.

Various approaches for the active control of acoustic fields have been proposed. For instance in [23] and [13], the design of active controls for acoustic cloaking was done using the Green representation Theorem for the Helmholtz equation. In [24] and [25], generalized Calderon potentials and boundary projection operators with quadratic functional optimization were used to construct the active acoustic controls. Multizone sound field synthesis and reproduction were studied using wave-domain methods (such as in [26,27]) or modal-domain approaches (see [28,29]). In a recent work [9], the authors studied and proposed an algorithm to mitigate the effect of bright zone scatterers on the overall multizone sound field synthesis effect. Boundary integral operators are used in [18] to produce a stable unified control strategy in the case of a single active surface source proving the active control of scalar fields in prescribed exterior region of space. These theoretical results were later applied for the 2D and 3D numerical study in [11,30,31]. Control problems for high frequency regimes that result in numerically unstable linear systems have been investigated using time-domain

* Corresponding author at: Institute of Mathematical Sciences and Physics, University of the Philippines Los Baños, Philippines.
E-mail address: naegarguin1@up.edu.ph (N.J.A. Egarguin).

https://doi.org/10.1016/j.wavemoti.2020.102523
0165-2125/

reformulations [32]. Other techniques that are used in the context of sound field control are discussed and analyzed in works such as [21,33,34] and [35].

Practical implementation of such strategies may involve the necessity of accurate field measurements or require the use of non-monopolar sources only. In this regard and in the context of scattered field active control, the authors in [24] and [36] proposed methods which are only based on measurements of the total field around the sources, while in a more general context, recently in [37], the authors proposed a method to overcome the difficult task of using monopolar sources in the control schemes proposed in the literature.

In our previous works, we studied the active manipulation of Helmholtz fields in two and three dimensions with the use of a single spherical source [11,18,30,31]. In these works, we considered well-separated control regions in space and using a single active compact source domain, approximated different a priori prescribed fields on each of these regions. This was done by finding the required inputs, either a normal velocity or the surface pressure on the boundary of the source necessary to produce a good approximation to the prescribed fields in each of the regions of control. The proposed scheme was based on a method of moments approach where a global basis representation for the required solutions was used (i.e., spherical harmonics) together with a Morozov discrepancy principle-based Tikhonov regularization. The method was shown to be accurate and robust against measurement noise and variations in the physical parameters of the problem geometry.

In this paper, we extend these results for the case of multiple compact source domains considering also the first order coupling effects. This can lead to applications such as the design of controllable arrays for multizone sound field synthesis, active noise cancellation, acoustic cloaking and shielding and acoustic contrast control design (see [38–40] and [41] for similar applications using loudspeaker arrays). Another novelty of the present work is the use of local instead of global basis functions (such as spherical harmonics) in the representation of the solution. This allowed for an easier representation of the solution on each array element and provided a greater flexibility for the shape of the sources.

The paper is organized as follows. In Section 2 we formally state the problem and develop the functional framework that will take into account the interaction between the sources. This section contains the main bulk of the paper's theoretical results. In Section 3, we present a theoretical stability result for our strategy which extends the results discussed in [30]. Then in Section 4, we present several numerical simulations validating our analysis. More explicitly, we present simulations using linear, planar and nonplanar array of sources with either two or three control regions which are bounded or have a bounded complement (i.e., unbounded far field region $\mathbb{R}^3 \setminus B_R(\mathbf{0})$, where $B_R(\mathbf{0})$ is the open ball centered at the origin of radius R). Lastly, Section 5 presents our conclusions and future research directions.

2. Statement of the problem and functional framework

Let $\mu \ll 1$ be a small positive parameter and let $\{R_1, R_2, \dots, R_m\}$ be a collection of m mutually disjoint smooth domains in $\mathbb{R}^3$ where R_m may possibly be the far field region $\mathbb{R}^3 \setminus B_R(\mathbf{0})$. We consider the problem of generating a prescribed acoustic field in R_l, $l = \overline{1,m}$ using a collection of active sources $\{D_1, D_2, \dots, D_n\}$ modeled as mutually disjoint compact regions in $\mathbb{R}^3$ with Lipschitz continuous boundaries. Mathematically, the problem is to find boundary inputs on these sources, either a Neumann input data $v_j \in C(\partial D_j)$ or a Dirichlet data $p_j \in C(\partial D_j)$ such that for any desired field $f = (f_1, f_2, \dots, f_m)$ on the control regions, the solution u of the following problem

$$\begin{cases} \Delta u + k^2 u = 0 \text{ in } \mathbb{R}^3 \setminus \left(\bigcup_{j=1}^{n} \overline{D_j} \right), \\ \nabla u \cdot \mathbf{n}_j = v_j, \text{ (or } u = p_j) \text{ on } \partial D_j, \ j = \overline{1,n} \\ \langle \hat{x}, \nabla u(x) \rangle - iku(x) = o\left(\frac{1}{|x|}\right), \text{ as } |x| \to \infty \text{ uniformly for all } \hat{x}, \end{cases} \tag{1}$$

satisfies

$$\|u - f_l\|_{C^2(R_l)} \leq \mu \text{ for } l = \overline{1,m} \tag{2}$$

where $C^2(M)$ denotes the space of functions defined on M with continuous partial derivatives up to the second order and here and throughout the rest of the paper $\mathbf{n}_j$ is the outward unit normal to $\partial D_j'$ and $\hat{x} = \frac{x}{|x|}$ denotes the unit vector along the direction x. As a convention, the $e^{-i\omega t}$ of the fields is implicitly assumed. It is well known that (see for example [42]) for every set of given Dirichlet or Neumann boundary inputs on $\bigcup_{j=1}^{n} \partial D_j$ problem (1) has a unique radiating solution $u \in C^2\left(\mathbb{R}^3 \setminus \bigcup_{j=1}^{n} \overline{D_j}\right) \cap C\left(\mathbb{R}^3 \setminus \bigcup_{j=1}^{n} D_j\right)$ (with the additional condition that the normal derivative exists in the sense of uniform convergence for the Neumann problem). This suggests that one way towards a possible solution is to consider a representation for the unique solution of the above exterior problem as a function of the inputs and study the possibility to characterize those boundary data which lead to a solution satisfying (2).

In [18], we considered a different approach and by using as an ansatz a layer potential representation for radiating exterior fields in the case of a single complex source, we showed that one can determine a class of densities for the layer potentials defined on the boundary of the source such that they approximate the field f_l on each control region R_l. This then led to a complete characterization of the required boundary inputs on the source (pressure or normal velocity) with the property that the field generated by them will satisfy (2) on the control regions. In fact if k is not a resonance (see [43] and [18,31]), the boundary input (normal velocity v or pressure p) on the single source D_1 can be characterized by a density w such that

$$v(x) = \frac{-i}{\rho c k}\frac{\partial}{\partial \mathbf{n}_1}\int_{\partial D_1'} w(y)\frac{\partial \phi(x,y)}{\partial \mathbf{n}_1}dS \text{ and} \tag{3}$$

$$p(x) = \int_{\partial D_1'} w(y)\frac{\partial \phi(x,y)}{\partial \mathbf{n}_1}dS, \tag{4}$$

where D_1' is a fictitious source that is compactly embedded in D_1. Although the expressions in (3) and (4) make use of the double layer potential operator, it was shown in [31] (see also [11]) that equally valid representations for the required boundary inputs could be obtained by using the single layer potential representation or more general, a representation given by a linear combination of single and double layer potentials.

In what follows we will present the extension of these results to the case of an array of sources factoring in the coupling among them. Let $A \subset\subset B$ denote the fact that A is compactly embedded in B. Consider fictitious sources $D_j' \subset\subset D_j, j = \overline{1,n}$, each of which is a smooth domain and let W_l for $l = \overline{1,m}$ be mutually disjoint open control regions with $R_l \subset\subset W_l$, for any l (where we additionally assume that if $R_m = \mathbb{R}^3 \setminus B_R(\mathbf{0})$ then W_m has a open connected complement). Further, we assume that the fictitious sources and the larger control regions are well separated, i.e.,

$$\overline{W_l} \cap \overline{D_j} = \emptyset, \text{ for } l = \overline{1,m} \text{ and } j = \overline{1,n}. \tag{5}$$

We define three product Hilbert spaces necessary for our analysis. First, we let

$$X = \prod_{j=1}^{n} L^2(\partial D_j'), \tag{6}$$

be the Hilbert space of n-tuples of L^2 functions on the surface of the fictitious sources endowed with the usual inner product

$$\langle v, w\rangle_X = \sum_{j=1}^{n}\langle v_j, w_j\rangle_{L^2(\partial D_j')} \tag{7}$$

for all $v = (v_1, v_2, \ldots, v_n)$, $w = (w_1, w_2, \ldots, w_n) \in X$. Then we define the product space

$$Y = \prod_{l=1}^{m} L^2(\partial W_l) \tag{8}$$

of m-tuples of L^2 functions on the surface of the slightly larger compact control regions with the inner product

$$\langle \varphi, \psi\rangle_Y = \sum_{l=1}^{m}\langle \varphi_l, \psi_l\rangle_{L^2(\partial W_l)} \tag{9}$$

for all $\varphi = (\varphi_1, \varphi_2, \ldots, \varphi_m)$ and $\psi = (\psi_1, \psi_2, \ldots, \psi_m) \in Y$. In order to account for the coupling between the sources, we need to consider each physical source as an evaluation region of the field generated by the other sources. Hence, for each $j = \overline{1,n}$, we define a third product Hilbert space

$$Z_j = \prod_{\substack{p=1\\ p\neq j}}^{n} L^2(\partial D_p) \tag{10}$$

of $n-1$-tuples of L^2 functions on the surface of the physical sources different from ∂D_j with the usual inner product

$$\langle f, g\rangle_{Z_j} = \sum_{\substack{p=1\\ p\neq j}}^{n}\langle f_p, g_p\rangle_{L^2(\partial D_p)} \tag{11}$$

for all $f = (f_1, \ldots, f_{j-1}, f_{j+1}, \ldots, f_n)$ and $g = (g_1, \ldots, g_{j-1}, g_{j+1}, \ldots, g_n) \in Z_j$. All other Hilbert spaces defined in the rest of this paper as a product of these spaces will assume the usual induced inner product analogous to the ones above.

Now following the framework laid down in [18], we can now define the propagator of each fictitious source (the field operator corresponding to each source). But aside from the control regions, we shall also design this operator to calculate

the generated field on the surface of each other physical source. Let ϕ be the fundamental solution of the Helmholtz equation in three dimensions:

$$\phi(x,y)=\frac{e^{ik|x-y|}}{4\pi|x-y|}. \tag{12}$$

and $\eta_1,\eta_2\in\mathbb{R}$ be the non-negative weights assigned to the double and single layer potential terms, respectively. Then for each $j=\overline{1,n}$ we define the operator

$$\mathcal{K}_j : L^2(\partial D_j')\to Y\times Z_j \tag{13}$$

such that for every density $w_j\in L^2(\partial D_j')$, and tuples of evaluation points $\mathbf{y}=(y_1,\dots,y_m)\in\prod_{l=1}^{m}\partial W_l$ and $\mathbf{z}=(z_1,\dots,z_{j-1},z_{j+1},\dots,z_n)\in\prod_{\substack{p=1\\p\neq j}}^{n}\partial D_p$ we have

$$\begin{aligned}&\mathcal{K}_j w_j(\mathbf{y},\mathbf{z})\\ &=\big(\mathcal{P}_{j1}w_j(y_1),\dots,\mathcal{P}_{jm}w_j(y_m),\mathcal{K}_{j1}w_j(z_1),\dots,\mathcal{K}_{j,j-1}w_j(z_{j-1}),\mathcal{K}_{j,j+1}w_j(z_{j+1}),\dots,\mathcal{K}_{jn}w_j(z_n)\big),\end{aligned} \tag{14}$$

where for each $l=\overline{1,m}$ and $s\in\partial W_l$

$$\mathcal{P}_{jl}w_j(s)=\eta_1\int_{\partial D_j'}w_j(x)\frac{\partial\phi(x,s)}{\partial\mathbf{n}_j}dS+i\eta_2\int_{\partial D_j'}w_j(x)\phi(x,s)dS, \tag{15}$$

and for every $p=\overline{1,n}$ with $p\neq j$ and $t\in\partial D_p$

$$\mathcal{K}_{jp}w_j(t)=\eta_1\int_{\partial D_j'}w_j(x)\frac{\partial\phi(x,t)}{\partial\mathbf{n}_j}dS+i\eta_2\int_{\partial D_j'}w_j(x)\phi(x,t)dS. \tag{16}$$

Note that the operators in Eqs. (15) and (16) are defined exactly in the same way but with different codomains. They both calculate the field propagated by source D_j due to the density $w_j\in L^2(\partial D_j')$. The operator $\mathcal{P}_{jl}$ evaluates this field at a point on the surface of the control region W_l while $\mathcal{K}_{jp}$ with $p\neq j$ computes the field at points on the surface of a physical source D_p.

From classical potential theory, both $\mathcal{P}_{jl}$ and $\mathcal{K}_{jp}$ as well as their respective adjoints $\mathcal{P}_{jl}^*$ and $\mathcal{K}_{jp}^*$ are all compact. It follows that $\mathcal{K}_j$ and its adjoint $\mathcal{K}_j^*$ are also compact.

The adjoint operator

$$\mathcal{K}_j^* : Y\times Z_j\to L^2(\partial D_j') \tag{17}$$

is defined such that for all $w\in L^2(\partial D_j')$ and $u=(\psi,\varphi)\in Y\times Z_j$ with $\psi=(\psi_1,\dots,\psi_m)\in Y$ and $\varphi=(\varphi_1,\dots,\varphi_{j-1},\varphi_{j+1},\dots,\varphi_n)\in Z_j$ the following holds:

$$\langle w,\mathcal{K}_j^*u\rangle_{L^2(\partial D_j')}=\langle\mathcal{K}_j w,u\rangle_{Y\times Z_j} \tag{18}$$

$$=\sum_{l=1}^{m}\langle\mathcal{P}_{jl}w,\psi_l\rangle_{L^2(\partial W_l)}+\sum_{\substack{p=1\\p\neq j}}^{n}\langle\mathcal{K}_{jp}w,\varphi_p\rangle_{L^2(\partial D_p)} \tag{19}$$

$$=\sum_{l=1}^{m}\langle w,\mathcal{P}_{jl}^*\psi_l\rangle_{L^2(\partial D_j')}+\sum_{\substack{p=1\\p\neq j}}^{n}\langle w,\mathcal{K}_{jp}^*\varphi_p\rangle_{L^2(\partial D_j')} \tag{20}$$

$$=\left\langle w,\sum_{l=1}^{m}\mathcal{P}_{jl}^*\psi_l\right\rangle_{L^2(\partial D_j')}+\left\langle w,\sum_{\substack{p=1\\p\neq j}}^{n}\mathcal{K}_{jp}^*\varphi_p\right\rangle_{L^2(\partial D_j')}. \tag{21}$$

Thus, for every such $u=(\psi,\varphi)\in Y\times Z_j$,

$$\mathcal{K}_j^*u=\sum_{l=1}^{m}\mathcal{P}_{jl}^*\psi_l+\sum_{\substack{p=1\\p\neq j}}^{n}\mathcal{K}_{jp}^*\varphi_p. \tag{22}$$

From [18], we have the following important property of $\mathcal{K}_j^*$ which by using classical linear operator theory directly implies that $\mathcal{K}_j$ has a dense range.

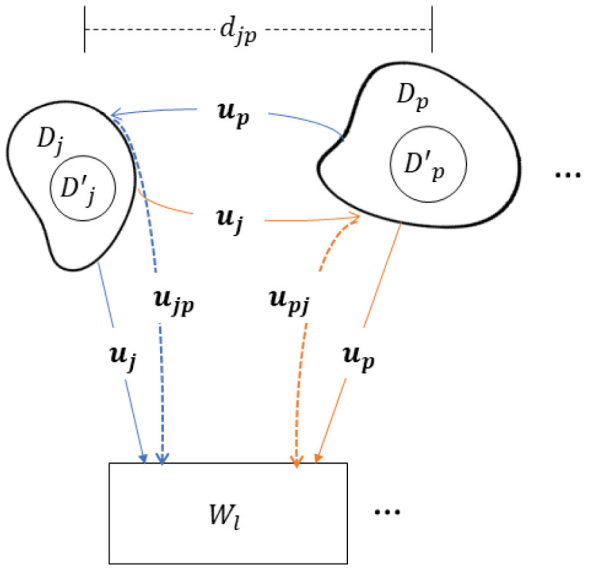

Fig. 1. Illustration of the first order coupling among sources.

Theorem 2.1 ([18]). *The operator $\mathcal{K}_j^*$ defined above has a trivial kernel, i.e, $\mathcal{K}_j^* u = \mathcal{K}_j^*(\psi, \varphi) = 0$ if and only if $\psi_l = 0$ for all $l = \overline{1, m}$ and $\varphi_p = 0$ for all $p = \overline{1, n}$, $p \neq j$.*

2.1. The coupling operator

The formulations above are extensions of the ones in [18] for the case of multiple sources and multiple control regions. The novelty of this work is the incorporation of the coupling among the sources into the model. In simple terms, coupling is the interaction between the sources in an array where the field radiated by one source is scattered by another source. Thus, the field generated by a source experiences some contributions from the other radiators in the array. These contributions are inversely proportional to the spacing between the sources in the array. Moreover, the contributions from higher order coupling, i.e., the contributions from the propagated field of a source onto another that bounces off one or more intermediate sources are assumed small.

Next, we shall only quantify the effects of first order coupling. Consider the geometric setting in Fig. 1, where we illustrate the first order coupling among sources. It shows the physical sources D_j and D_p with the respective embedded fictitious sources D'_j and D'_p and a control region W_l. These sources propagates the fields u_j and u_p, respectively not only onto the control region but also onto each other. In particular, as u_p hits the boundary ∂D_j it is scattered as a secondary field u_{jp}. Thus, the total field from ∂D_j propagated onto the control region is $u_j + u_{jp}$. Similarly. the total field from ∂D_p experienced by W_l is $u_p + u_{pj}$. This analysis can be extended to the case of more sources and more controls.

In order to characterize the contributions from the coupling among sources, we shall define the operators

$$\mathcal{S}_{jp} : L^2(\partial D'_p) \to L^2(\partial D'_j) \tag{23}$$

for $j, p = \overline{1, n}, j \neq p$ that will calculate the density w_{jp} on $\partial D'_j$ that will generate an approximation of the scattered field u_{jp}. Assuming that all sources have sound-soft boundaries, then u_{jp} satisfies

$$\begin{cases} \Delta u_{jp} + k^2 u_{jp} = 0, \text{ in } \mathbb{R}^3 \setminus \overline{D}_j \\ \langle \hat{x}, \nabla u_{jp}(x) \rangle - iku_{jp}(x) = o\left(\dfrac{1}{|x|}\right), \quad \text{as } |x| \to \infty \text{ uniformly for all } \hat{x} \\ u_{jp}(x) = -e^{ikd_{jp}} u_p(x), \qquad \text{for all } x \in \partial D_j. \end{cases} \tag{24}$$

where d_{jp} is the Euclidean distance between the centers of the fictitious spherical sources D'_j and D'_p and $e^{ikd_{jp}}$ is the associated delay factor. Note that the boundary condition of (24) is imposed on the surface of the actual physical source. Next, we define for every $j = \overline{1, n}$, the operator

$$\tilde{\mathcal{K}}_j : L^2(\partial D'_j) \to L^2(\partial D_j) \tag{25}$$

such that for every point $x \in \partial D_j$ and density $w_j \in L^2(\partial D'_j)$

$$\tilde{\mathcal{K}}_j w_j(x) = \eta_1 \int_{\partial D'_j} w_j(s) \frac{\partial \phi(s, x)}{\partial \mathbf{n}_j} dS + i\eta_2 \int_{\partial D'_j} w_j(s) \phi(s, x) dS. \tag{26}$$

This operator is defined in exactly the same way as $\mathcal{P}_{jl}$ and $\mathcal{K}_{jp}$ but with a different codomain. It evaluates the field on the surface of the physical source due to the fictitious source. This operator and its adjoint are both compact.

From [18], there exists an infinite family of densities $w_{jp} \in C(\partial D_j')$ such that

$$\tilde{\mathcal{K}}_j w_{jp} \approx u_{jp} = -e^{ikd_{jp}} u_p = -e^{ikd_{jp}} \mathcal{K}_{pj} w_p \tag{27}$$

where u_{jp} is the solution of (24) and in the last equality above we used the definition of u_p introduced above and the operators $\mathcal{K}_{pj}$ introduced at (16) which imply $u_p = \mathcal{K}_{pj} w_p$. The density w_{jp} can be taken to be the Tikhonov solution of (27) given by

$$w_{jp} = -e^{ikd_{jp}} (\alpha_{jp} I + \tilde{\mathcal{K}}_j^* \tilde{\mathcal{K}}_j)^{-1} \tilde{\mathcal{K}}_j^* \mathcal{K}_{pj} w_p \tag{28}$$

for some optimal choice of positive constant $\alpha_{jp} \ll 1$ and where I is the identity operator. Now we define $\mathcal{S}_{jp} : L^2(\partial D_p') \to L^2(\partial D_j')$ as the composite operator

$$\mathcal{S}_{jp} = -e^{ikd_{jp}} (\alpha_{jp} I + \tilde{\mathcal{K}}_j^* \tilde{\mathcal{K}}_j)^{-1} \tilde{\mathcal{K}}_j^* \mathcal{K}_{pj}. \tag{29}$$

We note that $\mathcal{S}_{jp}$ is compact, being a scalar multiple of the composition of the bounded operator $(\alpha_{jp} I + \tilde{\mathcal{K}}_j^* \tilde{\mathcal{K}}_j)^{-1}$ and compact operators $\tilde{\mathcal{K}}_j^*$ and $\mathcal{K}_p$. Consequently, its adjoint $\mathcal{S}_{jp}^* : L^2(\partial D_j') \to L^2(\partial D_p')$ given by

$$\mathcal{S}_{jp}^* = -e^{-ikd_{jp}} \mathcal{K}_{pj}^* \tilde{\mathcal{K}}_j (\alpha_{jp} I + \tilde{\mathcal{K}}_j^* \tilde{\mathcal{K}}_j)^{-1} \tag{30}$$

is also compact. In conclusion, (15) and the above discussion imply that $\mathcal{P}_{jl} \mathcal{S}_{jp} w_p(x)$ is a very good approximation of the propagated field at a point $x \in \partial W_l$ due to the scattering of u_p off the surface of D_j.

2.2. The propagator operator and its range

With the framework developed above, we can now define the propagator operator $\mathcal{D}$ that calculates the total field propagated on each control region as a superposition of the fields due to the n sources and the first order coupling among them. Define the operator $\mathcal{D} : X \to Y$ such that for every n-tuple of densities $w = (w_1, w_2, \ldots, w_n) \in X$ and m-tuple of evaluation points $\mathbf{y} = (y_1, y_2, \ldots, y_m) \in \prod_{l=1}^{m} \partial W_l$,

$$\mathcal{D} w(\mathbf{y}) = \big(\mathcal{D}_1 w(y_1), \mathcal{D}_2 w(y_2), \ldots, \mathcal{D}_m w(y_m)\big), \tag{31}$$

where for each $s \in \partial W_l$

$$\mathcal{D}_l w(s) = \sum_{j=1}^{n} \left[\mathcal{P}_{jl} w_j(s) + \sum_{\substack{p=1 \\ p \neq j}}^{n} \mathcal{P}_{jl} \mathcal{S}_{jp} w_p(s) \right] \tag{32}$$

The first term inside the outer summation in (32) represents the field propagated directly by the fictitious source D_j' due solely to its density w_j where P_{jl} was defined in (15). Meanwhile, the second term is a very good approximation of the totality of the fields that scatter off the surface of D_j due to first order coupling with the other sources D_p as discussed in Section 2.1. Hence, $\mathcal{D}$ is the operator that gives the total field on each control region due to the sources and the first-order coupling among them.

It is easy to see that each $\mathcal{D}_l, l = \overline{1, m}$ is compact. This immediately implies that $\mathcal{D}_l^*$, $\mathcal{D}$ and $\mathcal{D}^*$ are also compact operators. The following theorem establishes that $\mathcal{D}$ has a dense range, that is, for every $f \in Y$ and accuracy threshold $\mu > 0$, there is a density $w \in X$ such that

$$\|\mathcal{D} w - f\|_Y \leq \mu. \tag{33}$$

Theorem 2.2. *The compact operator $\mathcal{D}$ defined in (32) has a dense range.*

Proof. Since $\mathcal{D}$ is linear and compact, it suffices to show that $\mathcal{D}^*$ has a trivial kernel. Note that $\mathcal{D}^* : Y \to X$ is the operator that, for every $w \in X$ and $\psi = (\psi_1, \psi_2, \ldots, \psi_m) \in Y$, satisfies:

$$\langle w, \mathcal{D}^* \psi \rangle_X = \langle \mathcal{D} w, \psi \rangle_Y \tag{34}$$

$$= \sum_{l=1}^{m} \langle \mathcal{D}_l w, \psi_l \rangle_{L^2(\partial W_l)} \tag{35}$$

$$= \sum_{l=1}^{m} \left\langle \sum_{j=1}^{n} \left[\mathcal{P}_{jl} w_j + \sum_{\substack{p=1 \\ p \neq j}}^{n} \mathcal{P}_{jl} \mathcal{S}_{jp} w_p \right], \psi_l \right\rangle_{L^2(\partial W_l)} \tag{36}$$

$$= \sum_{l=1}^{m} \left[\left\langle \sum_{j=1}^{n} \mathcal{P}_{jl} w_j, \psi_l \right\rangle_{L^2(\partial W_l)} + \left\langle \sum_{j=1}^{n} \sum_{\substack{p=1 \\ p\neq j}}^{n} \mathcal{P}_{jl} \mathcal{S}_{jp} w_p, \psi_l \right\rangle_{L^2(\partial W_l)} \right]. \tag{37}$$

Note that

$$\sum_{l=1}^{m} \left\langle \sum_{j=1}^{n} \mathcal{P}_{jl} w_j, \psi_l \right\rangle_{L^2(\partial W_l)} = \sum_{j=1}^{n} \sum_{l=1}^{m} \left\langle w_j, \mathcal{P}_{jl}^* \psi_l \right\rangle_{L^2(\partial D_j')} \tag{38}$$

$$= \sum_{j=1}^{n} \left\langle w_j, \sum_{l=1}^{m} \mathcal{P}_{jl}^* \psi_l \right\rangle_{L^2(\partial D_j')} \tag{39}$$

and if $a_{jp} = \begin{cases} 1, & j \neq p \\ 0, & j = p \end{cases}$,

$$\sum_{l=1}^{m} \left\langle \sum_{j=1}^{n} \sum_{\substack{p=1 \\ p\neq j}}^{n} \mathcal{P}_{jl} \mathcal{S}_{jp} w_p, \psi_l \right\rangle_{L^2(\partial W_l)} = \sum_{l=1}^{m} \sum_{j=1}^{n} \sum_{\substack{p=1 \\ p\neq j}}^{n} \left\langle \mathcal{P}_{jl} \mathcal{S}_{jp} w_p, \psi_l \right\rangle_{L^2(\partial W_l)} \tag{40}$$

$$= \sum_{l=1}^{m} \sum_{j=1}^{n} \sum_{\substack{p=1 \\ p\neq j}}^{n} \left\langle w_p, \mathcal{S}_{jp}^* \mathcal{P}_{jl}^* \psi_l \right\rangle_{L^2(\partial D_p')} \tag{41}$$

$$= \sum_{j=1}^{n} \sum_{\substack{p=1 \\ p\neq j}}^{n} \left\langle w_p, \sum_{l=1}^{m} \mathcal{S}_{jp}^* \mathcal{P}_{jl}^* \psi_l \right\rangle_{L^2(\partial D_p')} \tag{42}$$

$$= \sum_{j=1}^{n} \sum_{p=1}^{n} \left\langle w_p, a_{jp} \sum_{l=1}^{m} \mathcal{S}_{jp}^* \mathcal{P}_{jl}^* \psi_l \right\rangle_{L^2(\partial D_p')} \tag{43}$$

$$= \sum_{p=1}^{n} \left\langle w_p, \sum_{j=1}^{n} \sum_{l=1}^{m} a_{jp} \mathcal{S}_{jp}^* \mathcal{P}_{jl}^* \psi_l \right\rangle_{L^2(\partial D_p')} \tag{44}$$

$$= \sum_{j=1}^{n} \left\langle w_j, \sum_{p=1}^{n} \sum_{l=1}^{m} a_{pj} \mathcal{S}_{pj}^* \mathcal{P}_{pl}^* \psi_l \right\rangle_{L^2(\partial D_j')} \tag{45}$$

$$= \sum_{j=1}^{n} \left\langle w_j, \sum_{\substack{p=1 \\ p\neq j}}^{n} \sum_{l=1}^{m} \mathcal{S}_{pj}^* \mathcal{P}_{pl}^* \psi_l \right\rangle_{L^2(\partial D_j')}. \tag{46}$$

Thus, using (39) and (46) in (37) gives

$$\langle w, \mathcal{D}^* \psi \rangle_X = \sum_{j=1}^{n} \left\langle w_j, \sum_{l=1}^{m} \mathcal{P}_{jl}^* \psi_l + \sum_{\substack{p=1 \\ p\neq j}}^{n} \sum_{l=1}^{m} \mathcal{S}_{pj}^* \mathcal{P}_{pl}^* \psi_l \right\rangle_{L^2(\partial D_j')}, \tag{47}$$

that is, $\mathcal{D}^* \psi = (\mathcal{D}_1^* \psi, \dots \mathcal{D}_n^* \psi)$ where for every $j = \overline{1, n}$,

$$\mathcal{D}_j^* \psi = \sum_{l=1}^{m} \mathcal{P}_{jl}^* \psi_l + \sum_{\substack{p=1 \\ p\neq j}}^{n} \sum_{l=1}^{m} \mathcal{S}_{pj}^* \mathcal{P}_{pl}^* \psi_l \tag{48}$$

$$= \sum_{l=1}^{m} \mathcal{P}_{jl}^* \psi_l + \sum_{\substack{p=1 \\ p\neq j}}^{n} \sum_{l=1}^{m} \left(-e^{-ikd_{pj}} \mathcal{K}_{jp}^* \tilde{\mathcal{K}}_p (\alpha_{pj} I + \tilde{\mathcal{K}}_p^* \tilde{\mathcal{K}}_p)^{-1} \right) \mathcal{P}_{pl}^* \psi_l \tag{49}$$

$$= \sum_{l=1}^{m} \mathcal{P}_{jl}^* \psi_l + \sum_{\substack{p=1 \\ p\neq j}}^{n} \mathcal{K}_{jp}^* \left[\sum_{l=1}^{m} \left(-e^{-ikd_{pj}} \tilde{\mathcal{K}}_p (\alpha_{pj} I + \tilde{\mathcal{K}}_p^* \tilde{\mathcal{K}}_p)^{-1} \right) \mathcal{P}_{pl}^* \psi_l \right] \tag{50}$$

$$= \mathcal{K}_j^* (\psi, \varphi) \tag{51}$$

where we used (22) with $\varphi = (\varphi_1, \dots, \varphi_{j-1}, \varphi_{j+1}, \dots, \varphi_n)$ with $\varphi_p = \sum_{l=1}^{m} \big(-e^{-ikd_{pj}} \tilde{\mathcal{K}}_p(\alpha_{pj} I + \tilde{\mathcal{K}}_p^* \tilde{\mathcal{K}}_p)^{-1}\big) \mathcal{P}_{pl}^* \psi_l$. Then from Theorem 2.1, $\psi \in \ker \mathcal{D}^*$ if and only if $\psi_l = 0$ for all $l = \overline{1, m}$. This and the compactness of $\mathcal{D}^*$ imply that $\mathcal{D}$ has a dense range. □

This theorem ensures the existence of a density $w = (w_1, w_2, \dots, w_n) \in X$ such that $\mathcal{D}w \approx f$. Moreover, each component w_j of w characterizes the required boundary input on the physical source D_j via the relations in (3) and (4) or their extensions.

3. Stability results

In this section, we discuss some regularization results that will lead to a stable solution of (1)–(2). Theorem 2.2 guarantees that for any $f \in Y$ there is a continuous function $w \in X$ such that $\mathcal{D}w \approx f$. However, we will be interested in regularized solutions, such as the minimum norm solution. Recall that for a bounded linear operator $T : A \to B$ and $f \in B$ the element $v_0 \in A$ is a minimum norm solution of $Tv = f$ with discrepancy μ if

$$\|Tv_0 - f\|_B \leq \mu$$

and

$$\|v_0\|_A = \inf_{\|Tv - f\|_B \leq \mu} \|v\|_A.$$

Theorem 2.2 and classical arguments (such as those in Chapter 16.4, [44]) imply the following result.

Corollary 3.1. *Let $\mathcal{D}$ be the operator defined in (32). Then for any $f \in Y$, the equation*

$$\mathcal{D}w = f \tag{52}$$

has a minimum norm solution in X.

Thus, for any $f = (f_1, f_2, \dots, f_m) \in Y$ we can choose the density $w^\alpha \in X$ to be the Tikhonov solution, that is the minimizer of the discrepancy functional

$$F(w, \alpha) = \sum_{l=1}^{m} \beta_l \|\mathcal{D}_l w - f_l\|^2_{L^2(\partial W_l)} + \alpha \|w\|^2_X \tag{53}$$

where

$$\beta_l = \begin{cases} \dfrac{1}{\|f_l\|^2_{L^2(\partial W_l)}}, & \text{if } f_l \neq 0 \\ 1, & \text{if } f_l = 0, \text{ and } W_l \text{ is bounded} \\ \dfrac{1}{4\pi R^2}, & \text{if } f_l = 0 \text{ and } W_l = \mathbb{R}^3 \setminus B_R(\mathbf{0}), \end{cases} \tag{54}$$

and the regularization parameter α is computed following the Morozov discrepancy principle, i.e., as the solution of

$$F(w, \alpha) = \delta^2, \tag{55}$$

for some prescribed accuracy threshold $\delta \ll 1$. With this choice of w^α, we obtain the following stability results analogous to the ones established in [30].

Lemma 3.1. *Let $0 < \delta < \dfrac{1}{\sqrt{2}}$ and w^α be the Tikhonov solution of (52) with respect to the discrepancy functional F defined in (53) . If $F(w^\alpha) \leq \delta^2$ then for each $l = \overline{1, m}$,*

$$\|f_l\|_{L^2(\partial W_l)} \leq 4 \|(\mathcal{D}_l)^*\|_O \|w^\alpha\|_X, \tag{56}$$

where $\|\cdot\|_O$ denotes the operatorial norm.

Proof. If $f_l = 0$, then (56) is trivial. Assume that $f_l \neq 0$. Since $F(w^\alpha) \leq \delta^2$,

$$\delta^2 \|f_l\|^2_{L^2(\partial W_l)} \geq \|\mathcal{D}_l w^\alpha - f_l\|^2_{L^2(\partial W_l)} \tag{57}$$

$$= \|\mathcal{D}_l w^\alpha\|^2_{L^2(\partial W_l)} - 2 \operatorname{Re} \langle \mathcal{D}_l w^\alpha, f_l \rangle_{L^2(\partial W_l)} + \|f_l\|^2_{L^2(\partial W_l)}. \tag{58}$$

Then it follows that

$$(1 - \delta^2) \|f_l\|^2_{L^2(\partial W_l)} \leq 2 \operatorname{Re} \langle \mathcal{D}_l w^\alpha, f_l \rangle_{L^2(\partial W_l)} \tag{59}$$

$$= 2\ \mathrm{Re}\langle w^{\alpha}, (\mathcal{D}_l)^* f_l\rangle_X \tag{60}$$

$$\leq 2\|w^{\alpha}\|_X \|(\mathcal{D}_l)^* f_l\|_X \tag{61}$$

and so

$$(1-\delta^2)\|f_l\|_{L^2(\partial W_l)} \leq 2\|w^{\alpha}\|_X \frac{\|(\mathcal{D}_l)^* f_l\|_X}{\|f_l\|_{L^2(\partial W_l)}} \leq 2\|w^{\alpha}\|_X \|(\mathcal{D}_l)^*\|_O \tag{62}$$

$$\Longrightarrow \|w^{\alpha}\|_X \geq \frac{(1-\delta^2)\|f_l\|_{L^2(\partial W_l)}}{2\|(\mathcal{D}_l)^*\|_O} \geq \frac{\|f_l\|_{L^2(\partial W_l)}}{4\|(\mathcal{D}_l)^*\|_O}. \tag{63}$$

Therefore, $\|f_l\|_{L^2(\partial W_l)} \leq 4\|(\mathcal{D}_l)^*\|_O \|w^{\alpha}\|_X$. □

This lemma provides a key inequality needed for our stability result. Without loss of generality, we assume that $f = (f_1, f_2, \ldots, f_{m^*}, \ldots, f_m)$ with $f_l \neq 0$ for all $l \leq m^*$ and $f_l = 0$ for $l = \overline{m^*+1, m}$. We consider a perturbation f^{ϵ} of f with magnitude $\epsilon > 0$ and

$$f^{\epsilon} = f + \epsilon s = (f_1 + \epsilon s_1, f_2 + \epsilon s_2, \ldots, f_{m^*} + \epsilon s_{m^*}, f_{m^*+1}, \ldots, f_m), \tag{64}$$

where $s \in Y$ is a random perturbation with

$$\|s_l\|_{L^2(\partial W_l)} \leq C\|f_l\|_{L^2(\partial W_l)} \tag{65}$$

for some constant C and all $l = \overline{1, m^*}$. Further, we let w^{α_0} be the Tikhonov solution of the unperturbed equation (52) and w^{α_ϵ} be the Tikhonov solution of

$$\mathcal{D}w = f^{\epsilon}. \tag{66}$$

Moreover, we denote the corresponding discrepancy functional for the perturbed system by

$$G(\alpha, \epsilon) = \sum_{l=1}^{m} \beta_l^{\epsilon} \|\mathcal{D}_l w^{\alpha_\epsilon} - f_l^{\epsilon}\|^2_{L^2(\partial W_l)} + \alpha \|w^{\alpha_\epsilon}\|^2_X \tag{67}$$

where β_l^{ϵ} is defined as in (54) with f_l replaced by f_l^{ϵ}. We want to show that the relative difference between the solutions w^{α_0} and w^{α_ϵ} is at most a multiple of the magnitude ϵ. The next proposition provides an upper bound for this relative difference.

Proposition 3.1. *Let $0 < \delta < \frac{1}{\sqrt{2}}$ and f^{ϵ} be as defined in (64). For every $\epsilon > 0$, let w^{α_ϵ} be the Tikhonov solution of $\mathcal{D}w = f^{\epsilon}$ such that $G(\alpha, \epsilon) = \delta^2$. Then*

$$\frac{\|w^{\alpha_\epsilon} - w^{\alpha_0}\|_X}{\|w^{\alpha_\epsilon}\|_X} \leq \frac{\frac{C\epsilon}{\alpha_0\lambda}\left(1+\frac{\delta}{\sqrt{\alpha_0}}\right) + \left|\frac{\alpha_\epsilon}{\alpha_0} - 1\right| + \sqrt{\left(\frac{C\epsilon}{\alpha_0\lambda}\left(1+\frac{\delta}{\sqrt{\alpha_0}}\right) + \left|1 - \frac{\alpha_\epsilon}{\alpha_0}\right|\right)^2 + 4\epsilon C\frac{\delta+\epsilon}{\alpha_0\lambda^2}}}{2} \tag{68}$$

where C and λ are generic positive constants independent of ϵ, δ and α_0.

Proof. Note that the solutions w^{α_ϵ} and w^{α_0} satisfy

$$\begin{cases} \alpha_0 w^{\alpha_0} + \tilde{\mathcal{D}}^*\tilde{\mathcal{D}} w^{\alpha_0} & = \tilde{\mathcal{D}}^* \tilde{f} \\ \alpha_\epsilon w^{\alpha_\epsilon} + \tilde{\mathcal{D}}_\epsilon^*\tilde{\mathcal{D}}_\epsilon w^{\alpha_\epsilon} & = \tilde{\mathcal{D}}_\epsilon^* \tilde{\tilde{f}}^{\epsilon} \end{cases}$$

$$\Longrightarrow \alpha_0 w^{\alpha_0} - \alpha_\epsilon w^{\alpha_\epsilon} + \tilde{\mathcal{D}}_\epsilon^*\tilde{\mathcal{D}}_\epsilon(w^{\alpha_0} - w^{\alpha_\epsilon}) = \tilde{\mathcal{D}}^*(\tilde{f} - \tilde{f}^{\epsilon}) + \tilde{\mathcal{D}}^*(\tilde{f}^{\epsilon} - \tilde{\tilde{f}}^{\epsilon}) + (\tilde{\mathcal{D}}^* - \tilde{\mathcal{D}}_\epsilon^*)\tilde{\tilde{f}}^{\epsilon} + (\tilde{\mathcal{D}}_\epsilon^*\tilde{\mathcal{D}}_\epsilon - \tilde{\mathcal{D}}^*\tilde{\mathcal{D}}) w^{\alpha_0} \tag{69}$$

with

$$\begin{aligned} \tilde{\tilde{f}}^{\epsilon} &= (\sqrt{\beta_1^{\epsilon}} f_1^{\epsilon}, \sqrt{\beta_2^{\epsilon}} f_2^{\epsilon}, \ldots, \sqrt{\beta_m^{\epsilon}} f_m^{\epsilon}) \\ \tilde{f} = (\sqrt{\beta_1} f_1, \sqrt{\beta_2} f_2, \ldots, \sqrt{\beta_m} f_m), \tilde{f}^{\epsilon} &= (\sqrt{\beta_1} f_1^{\epsilon}, \sqrt{\beta_2} f_2^{\epsilon}, \ldots, \sqrt{\beta_m} f_m^{\epsilon}) \\ \tilde{\mathcal{D}} w &= \left(\sqrt{\beta_1}\mathcal{D}_1 w, \sqrt{\beta_2}\mathcal{D}_2 w, \ldots, \sqrt{\beta_m}\mathcal{D}_m w\right) \text{for } w \in X \\ \tilde{\mathcal{D}}^* \psi &= \left(\sqrt{\beta_1}\mathcal{D}_1^* \psi, \sqrt{\beta_2}\mathcal{D}_2 \psi, \ldots, \sqrt{\beta_m}\mathcal{D}_m \psi\right) \text{ for } \psi \in Y \end{aligned} \tag{70}$$

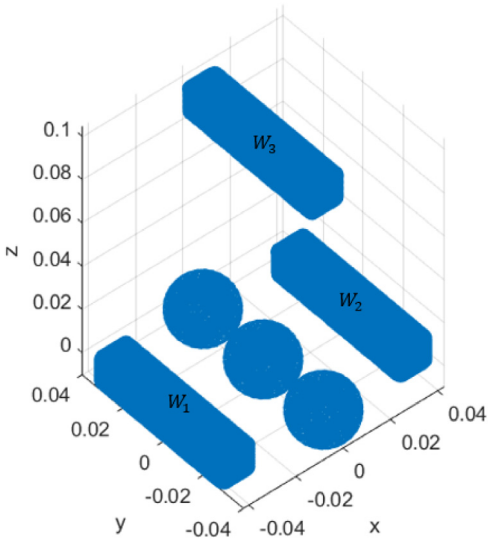

Fig. 2. Illustration of the simulation geometry.

and $\mathcal{D}_1, \mathcal{D}_2, \ldots, \mathcal{D}_m$ as introduced in (31). Integrating both sides of (69) against $w^{\alpha_0} - w^{\alpha_\epsilon}$ yields

$$\begin{aligned}
&\alpha_0 \|w^{\alpha_0} - w^{\alpha_\epsilon}\|_X^2 + (\alpha_0 - \alpha_\epsilon)\, \langle w^{\alpha_\epsilon}, w^{\alpha_0} - w^{\alpha_\epsilon}\rangle_X + \|\tilde{\mathcal{D}}_\epsilon(w^{\alpha_0} - w^{\alpha_\epsilon})\|_Y^2 \\
&\quad \leq \left\langle \tilde{f} - \tilde{f}^\epsilon, \tilde{\mathcal{D}}(w^{\alpha_0} - w^{\alpha_\epsilon}) \right\rangle_Y + C\epsilon \left(1 + \frac{\delta}{\sqrt{\alpha_0}}\right) \|(w^{\alpha_0} - w^{\alpha_\epsilon})\|_X
\end{aligned} \tag{71}$$

where for the last term on the right hand side of (71) we have used elementary algebraic manipulations, the definition of the operators $\tilde{\mathcal{D}}, \tilde{\mathcal{D}}^*, \tilde{\mathcal{D}}_\epsilon, \tilde{\mathcal{D}}_\epsilon^*$ and their boundedness independent of ϵ, the fact that $\|w_{\alpha_0}\|_X \leq \frac{\delta}{\sqrt{\alpha_0}}$ (immediate consequence of (55)), and the immediate estimate $|\beta_l^\epsilon - \beta_l| \leq C\epsilon$ for some generic positive constant C independent of ϵ, δ and α_0. Inequality (71) further implies

$$\begin{aligned}
\alpha_0 \|w^{\alpha_0} - w^{\alpha_\epsilon}\|_X^2 &\leq \left\langle \tilde{f} - \tilde{f}^\epsilon, \tilde{\mathcal{D}}(w^{\alpha_0} - w^{\alpha_\epsilon}) \right\rangle_Y + C\epsilon \left(1 + \frac{\delta}{\sqrt{\alpha_0}}\right) \|w^{\alpha_0} - w^{\alpha_\epsilon}\|_X - (\alpha_0 - \alpha_\epsilon)\, \langle w^{\alpha_\epsilon}, w^{\alpha_0} - w^{\alpha_\epsilon}\rangle_X \\
&= \sum_{l=1}^{m} \beta_l \left\langle f_l - f_l^\epsilon, \mathcal{D}_l(w^{\alpha_0} - w^{\alpha_\epsilon}) \right\rangle_{L^2(\partial W_l)} + C\epsilon \left(1 + \frac{\delta}{\sqrt{\alpha_0}}\right) \|w^{\alpha_0} - w^{\alpha_\epsilon}\|_X - (\alpha_0 - \alpha_\epsilon) \langle w^{\alpha_\epsilon}, w^{\alpha_0} - w^{\alpha_\epsilon}\rangle_X .
\end{aligned}$$

Recall that it was assumed that $f_l \neq 0$ for all $l \leq m^*$ and $f_l = 0$ for $l = \overline{m^* + 1, m}$. Also note that if $f_l = 0$ then $f_l^\epsilon = 0$. So,

$$\begin{aligned}
\alpha_0 \|w^{\alpha_0} - w^{\alpha_\epsilon}\|_X^2 &\leq \sum_{l=1}^{m^*} \beta_l \left\langle f_l - f_l^\epsilon, \mathcal{D}_l(w^{\alpha_0} - w^{\alpha_\epsilon}) \right\rangle_{L^2(\partial W_l)} \\
&\quad + C\epsilon \left(1 + \frac{\delta}{\sqrt{\alpha_0}}\right) \|w^{\alpha_0} - w^{\alpha_\epsilon}\|_X - (\alpha_0 - \alpha_\epsilon)\, \langle w^{\alpha_\epsilon}, w^{\alpha_0} - w^{\alpha_\epsilon}\rangle_X \\
&\leq \sum_{l=1}^{m^*} \beta_l \|f_l - f_l^\epsilon\|_{L^2(\partial W_l)} \|\mathcal{D}_l(w^{\alpha_0} - w^{\alpha_\epsilon})\|_{L^2(\partial W_l)} \\
&\quad + C\epsilon \left(1 + \frac{\delta}{\sqrt{\alpha_0}}\right) \|w^{\alpha_0} - w^{\alpha_\epsilon}\|_X - (\alpha_0 - \alpha_\epsilon)\, \langle w^{\alpha_\epsilon}, w^{\alpha_0} - w^{\alpha_\epsilon}\rangle_X .
\end{aligned} \tag{72}$$

Note that from (65), $\|f_l - f_l^\epsilon\|_{L^2(\partial W_l)} = \|\epsilon s_l\|_{L^2(\partial W_l)} \leq \epsilon C \|f_l\|_{L^2(\partial W_l)}$. Using this and (57) from the proof of Lemma 3.1, we have

$$\begin{aligned}
\|\mathcal{D}_l(w^{\alpha_0} - w^{\alpha_\epsilon})\|_{L^2(\partial W_l)} &= \|\mathcal{D}_l w^{\alpha_0} - f_l - \mathcal{D}_l w^{\alpha_\epsilon} + f_l^\epsilon + f_l - f_l^\epsilon\|_{L^2(\partial W_l)} \\
&\leq \|\mathcal{D}_l w^{\alpha_0} - f_l\|_{L^2(\partial W_l)} + \|\mathcal{D}_l w^{\alpha_\epsilon} - f_l^\epsilon\|_{L^2(\partial W_l)} + \|f_l - f_l^\epsilon\|_{L^2(\partial W_l)} \\
&\leq (2\delta + \epsilon C) \|f_l\|_{L^2(\partial W_l)}.
\end{aligned} \tag{73}$$

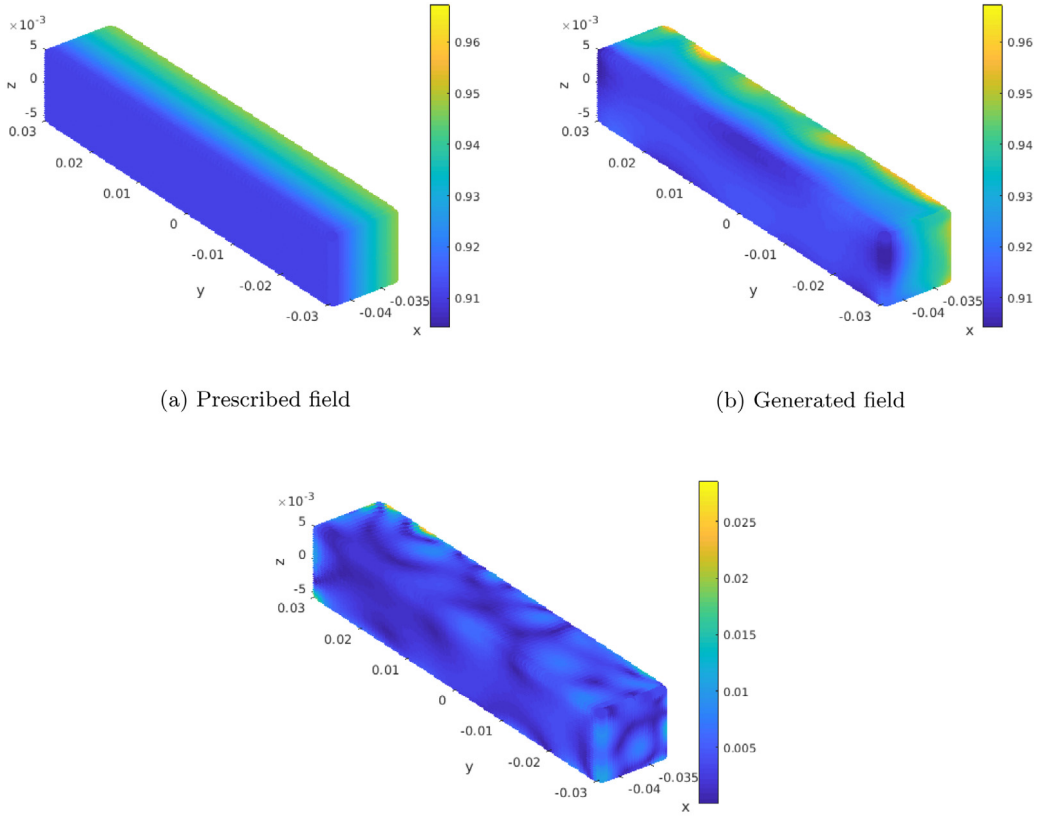

(a) Prescribed field

(b) Generated field

(c) Pointwise relative error

Fig. 3. Results of the pattern synthesis on W_1.

Thus, (72) becomes

$$\begin{aligned}\alpha_0\|w^{\alpha_0}-w^{\alpha_\epsilon}\|_X^2 &\le \sum_{l=1}^{m^*}\beta_l\left[\epsilon C\|f_l\|_{L^2(\partial W_l)}(2\delta+\epsilon C)\|f_l\|_{L^2(\partial W_l)}\right]\\ &\quad + C\epsilon\left(1+\frac{\delta}{\sqrt{\alpha_0}}\right)\|w^{\alpha_0}-w^{\alpha_\epsilon}\|_X-(\alpha_0-\alpha_\epsilon)\langle w^{\alpha_\epsilon},w^{\alpha_0}-w^{\alpha_\epsilon}\rangle_X\\ &\le \epsilon C\frac{(\delta+\epsilon)}{\lambda^2}\|w^{\alpha_\epsilon}\|_X^2+\left(\frac{C\epsilon}{\lambda}\left(1+\frac{\delta}{\sqrt{\alpha_0}}\right)+|\alpha_0-\alpha_\epsilon|\right)\|w^{\alpha_\epsilon}\|_X\|w^{\alpha_0}-w^{\alpha_\epsilon}\|_X\end{aligned}\tag{74}$$

where we made use of (54) in the second inequality above and employed Lemma 3.1 for w_{α_ϵ} and the boundedness of $\tilde{\mathcal{D}}_\epsilon^*$ with respect to ϵ to obtain the existence of a $\lambda>0$ independent of ϵ such that $\|w^{\alpha_\epsilon}\|_X\ge\max_l\dfrac{\|f_l^\epsilon\|_{L^2(\partial W_l)}}{4\|(\mathcal{D}_l^\epsilon)^*\|_O}\ge\lambda$. Defining, $A=\dfrac{\|w^{\alpha_\epsilon}-w^{\alpha_0}\|_X}{\|w^{\alpha_\epsilon}\|_X}$, (74) implies

$$\alpha_0A^2\le\left(\frac{C\epsilon}{\lambda}\left(1+\frac{\delta}{\sqrt{\alpha_0}}\right)+|\alpha_0-\alpha_\epsilon|\right)A+\epsilon C\frac{(\delta+\epsilon)}{\lambda^2}$$

$$\implies A^2-\left(\frac{C\epsilon}{\alpha_0\lambda}\left(1+\frac{\delta}{\sqrt{\alpha_0}}\right)+|1-\frac{\alpha_\epsilon}{\alpha_0}|\right)A-\epsilon C\frac{(\delta+\epsilon)}{\alpha_0\lambda^2}\le 0.\tag{75}$$

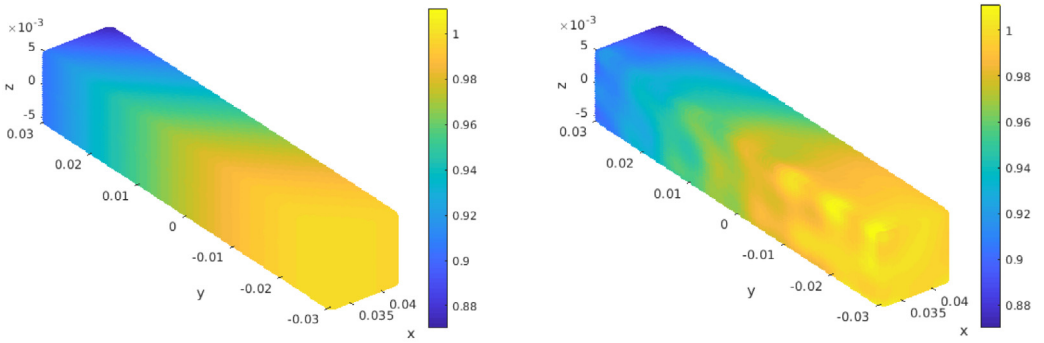

(a) Prescribed field

(b) Generated field

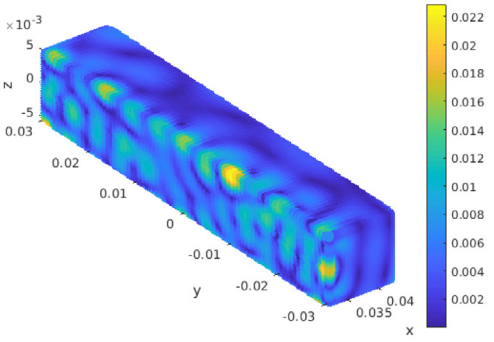

(c) Pointwise relative error

Fig. 4. Results of the pattern synthesis on W_2.

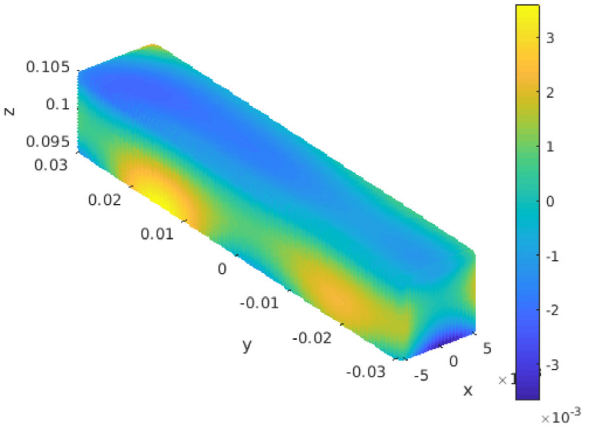

Fig. 5. Real part of the generated field on W_3.

Finally from (75) we obtain the desired inequality

$$A \leq \frac{\frac{C\epsilon}{\alpha_0\lambda}\left(1+\frac{\delta}{\sqrt{\alpha_0}}\right)+\left|\frac{\alpha_\epsilon}{\alpha_0}-1\right|+\sqrt{\left(\frac{C\epsilon}{\alpha_0\lambda}\left(1+\frac{\delta}{\sqrt{\alpha_0}}\right)+\left|1-\frac{\alpha_\epsilon}{\alpha_0}\right|\right)^2+4\epsilon C\frac{\delta+\epsilon}{\alpha_0\lambda^2}}}{2}. \quad \square \tag{76}$$

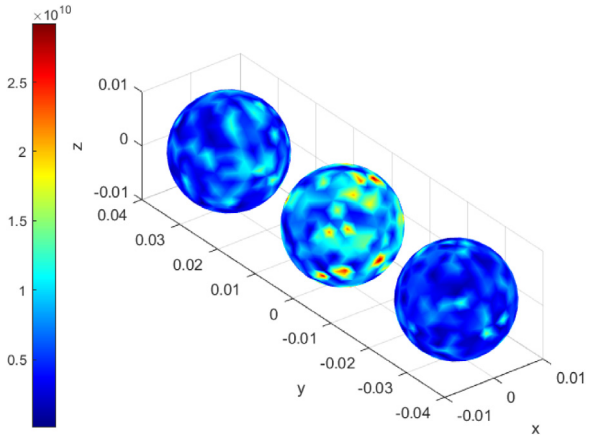

Fig. 6. Pointwise magnitude of the density w.

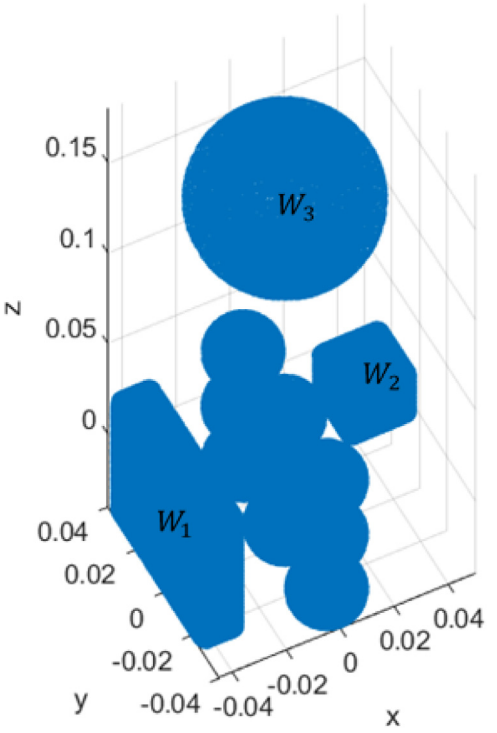

Fig. 7. Illustration of the simulation geometry.

Remark 3.1. Note that by using the continuity of $\alpha(\epsilon) = \alpha_\epsilon$ as a function of ϵ as $\epsilon \ll 1$ (consequence of implicit function theorem, see also [30]), Proposition 3.1 implies that for fixed accuracy level δ the Tikhonov solution proposed in our scheme is stable with respect to the noise level ϵ.

4. Numerical implementation

In this section we propose a numerical implementation of the solution scheme for (1)–(2) developed in the previous sections. We begin by discussing the discretization scheme leading to the formulation of the corresponding linear system. Then we show some results of the numerical simulations under various geometric configurations.

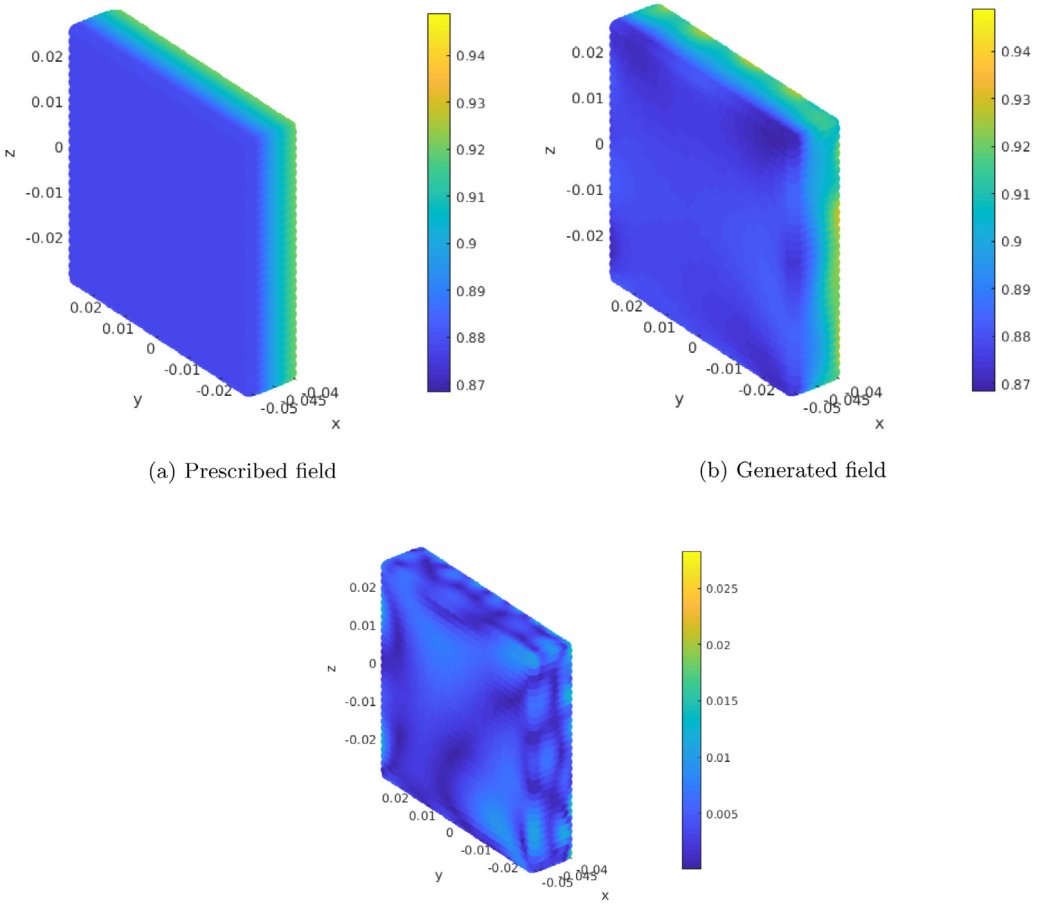

(a) Prescribed field

(b) Generated field

(c) Pointwise relative error

Fig. 8. Results of the pattern synthesis on W_1.

4.1. Discretization

In [31] and [11], numerical solutions to (1)–(2) were presented in the case of a single source. Moreover, the density w characterizing the necessary boundary data was approximated by the truncated series

$$w^{\alpha}(x) = \sum_{l=0}^{L} \sum_{p=-l}^{l} c_{pl} Y_l^p(\hat{x}), \text{ for } x \in \partial D_1' \tag{77}$$

of spherical harmonics Y_l^p (see [42,45]). Thus, the problem of finding the density $w \in L^2(\partial D_1')$ was reduced to finding a discrete set of coefficients c_{pl}. The expansion in (77), the orthogonality of the spherical harmonics and the addition theorem for spherical harmonics provided an analytic way of computing $\mathcal{D}w^{\alpha}$ without performing any integration. This resulted into a fast and accurate way of discretizing $\mathcal{D}w = f$. This expansion relies on the spherical coordinates with respect to the center of the fictitious spherical source D_1'. Thus, if one wishes to use this approach for the case of multiple sources, the expansion for each w_j^{α} should be computed with respect to a center common to all sources by employing addition theorems (see for instance [46] for a related work for electromagnetic waves). In this paper, we use local basis functions to reduce the integral equation $\mathcal{D}w = f$ to a linear system $Ac = b$. This will not only avoid the use of addition theorems to find the appropriate spherical harmonic decomposition of the densities on each fictitious source but will, in general, also allow the sources to assume arbitrary shapes. In the numerical simulations below, we use nodal local basis functions defined on triangular elements. A detailed discussion of local basis functions applied to finite element methods in acoustics and electromagnetics can be found in [47]. We first discretize the surface of each fictitious source D_j' into a set $\{T_j^1, T_j^2, \ldots, T_j^N\}$ of triangular elements such that each vertex of the triangle lies on the surface of the fictitious source. Then for each vertex v_i of qth triangle T_j^q, we associate a linear interpolating function N_i such that $N_i(v_i) = 1$ and zero on

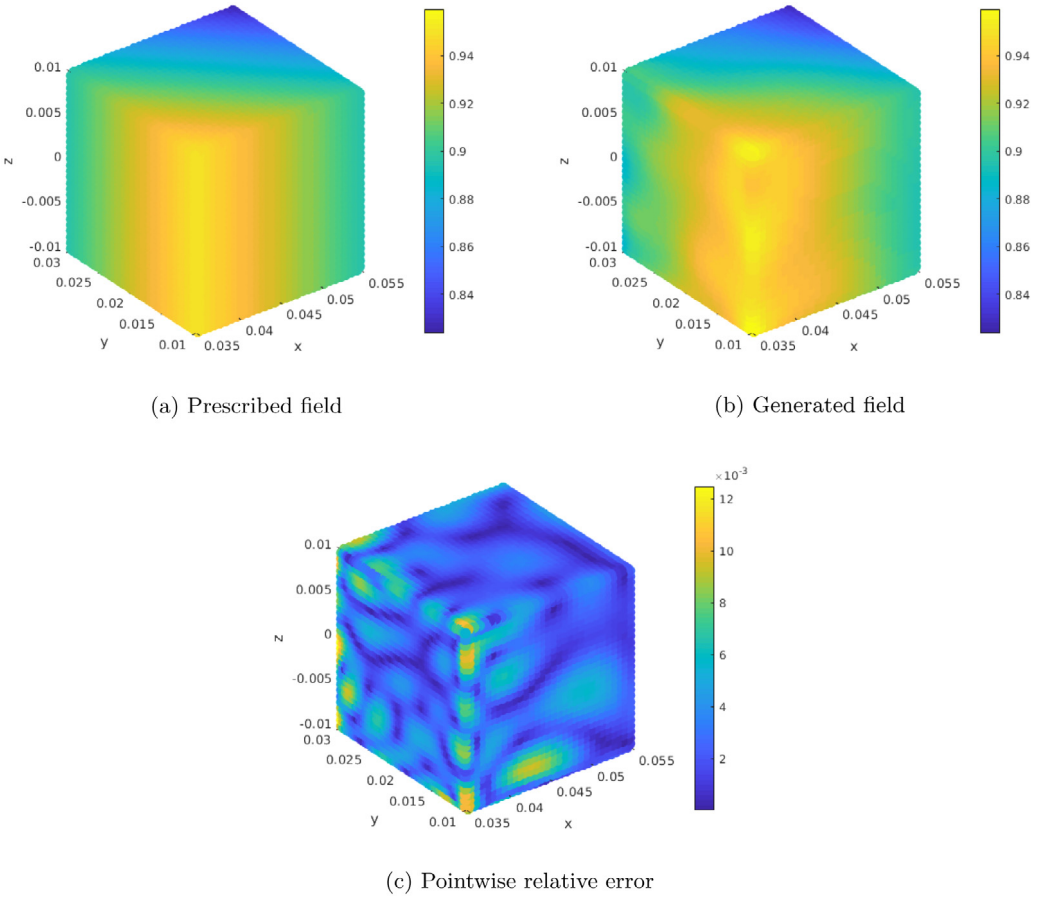

(a) Prescribed field

(b) Generated field

(c) Pointwise relative error

Fig. 9. Results of the pattern synthesis on W_2.

the other two vertices. Thus, for every $x \in T_j^q$, the unknown density function w_j^α can be expressed by the linear interpolant

$$w_{j,q}^\alpha(x) = \sum_{i=1}^{3} c_i N_i(x), \tag{78}$$

where the coefficient c_i is the value of w_j^α on vertex v_i. Thus, the problem of finding the unknown function $w^\alpha = (w_1^\alpha, w_2^\alpha, \ldots, w_n^\alpha) \in X$ is reduced to solving for the coefficients c_i's.

With a mesh of triangular elements approximating each of the fictitious sources, expressing w^α as the continuous piecewise function defined by the pieces in (78) and discretizing every control region, the operatorial equation $\mathcal{D}w = f$ considered first on a set of collocation test points, can then be approximated by the linear system $Ac = b$. Suppose that there are a total of m discretization points on the control regions and a total of n points on the surface of the fictitious sources. Then the matrices A, c and b are of dimensions $m \times n$, $n \times 1$ and $m \times 1$, respectively. Each entry of the matrix A is an integral approximated using the standard seven-point Gaussian quadrature rule. Then the unknown vector c of basis coefficients is computed as the Tikhonov solution

$$c = (\alpha I + A^*A)^{-1}A^*b \tag{79}$$

with the regularization parameter α chosen using the Morozov discrepancy principle.

In the succeeding sections, we present several implementations of the scheme discussed above under different geometric configurations. In all cases, the wave number is $k = 10$. Unless stated otherwise, 419 basis functions were used on each spherical fictitious source modeling the actual physical source. In all simulations, we gauge the accuracy of the obtained solutions by looking at the generated fields at prescribed sets of evaluation points on the control regions. As a computational stability check, these evaluation points are chosen to be the midpoint between consecutive points in the original mesh of collocation points used together with the local basis discretization to obtain the solution (79) to the associated linear system. We present visual comparisons of the prescribed field f_l and generated field u_l, the pointwise

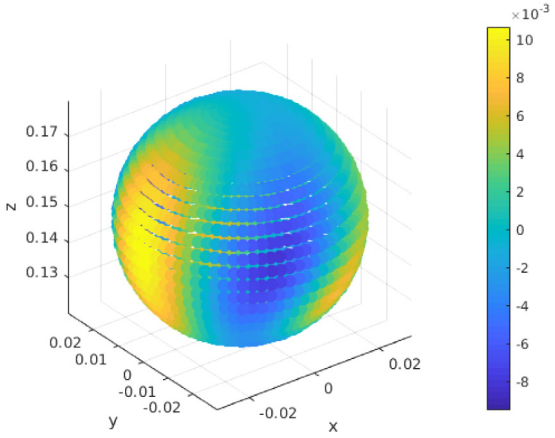

Fig. 10. Real part of the generated field on W_3.

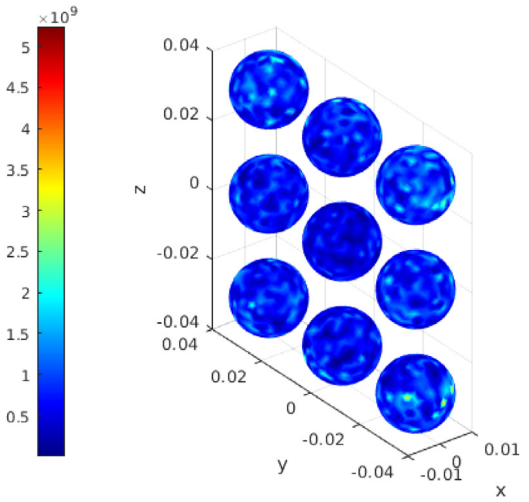

Fig. 11. Pointwise magnitude of the density w.

relative error $\frac{|f_l(x) - u_l(x)|}{|f_l(x)|}$ for each evaluation point x and the overall L^2 relative error computed as

$$\frac{\|f_l - u_l\|_{L^2(\partial W_l)}}{\|f_l\|_{L^2(\partial W_l)}} \tag{80}$$

for each control W_l whenever $f_l \neq 0$. Whenever creating a null field on W_l, we observe the L^2 norm of the field, the supremum magnitude of the field on the control and the relative contrast $C_{ll'}$ of the norm of f_l against the generated field $f_{l'} \neq 0$ on another control $W_{l'}$ calculated as

$$C_{ll'} = \frac{\frac{1}{|W_l|}\|f_l\|_{L^2(\partial W_l)}}{\frac{1}{|W_{l'}|}\|f_{l'}\|_{L^2(\partial W_{l'})}}, \tag{81}$$

which we want to be as close to zero as possible.

4.2. Linear array of sources

In this simulation, we consider three sources represented by three spherical fictitious sources arranged in a line. All fictitious sources have radius 0.01 m and are centered on the points $(0, 0, 0)$, $(0, -0.03, 0)$ and $(0, 0.03, 0)$. Also, we use

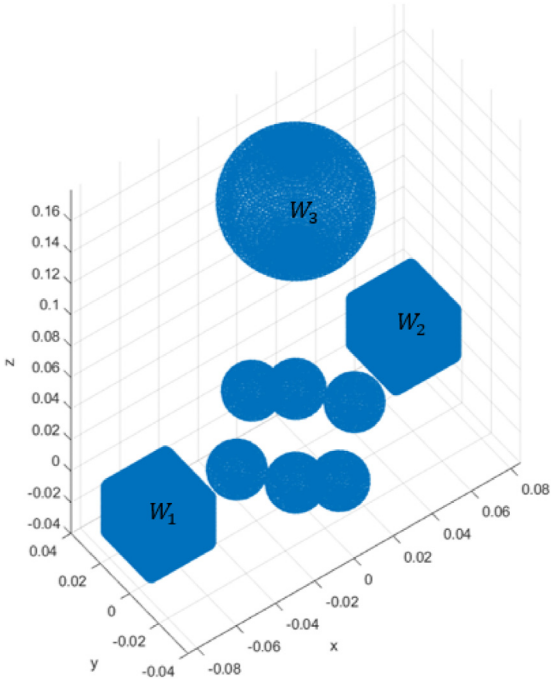

Fig. 12. Illustration of the simulation geometry.

three rectangular slabs of dimensions $0.01 \times 0.06 \times 0.01$ with centers at $(-0.0375, 0, 0)$, $(0.0375, 0, 0)$ and $(0, 0, 0.1)$ as the control regions W_1, W_2 and W_3 respectively. This geometric configuration is shown in Fig. 2.

Each source is sampled by 419 points, each serving as a vertex of some triangular elements. Each control region is discretized into 16000 points. In W_1 we prescribe the plane wave $f_1(\mathbf{x}) = e^{i\mathbf{x}\cdot(-10\hat{\mathbf{e}}_1)}$ and in W_2, the plane wave $f_2(\mathbf{x}) = e^{i\mathbf{x}\cdot(10\hat{\mathbf{d}})}$ where here and throughout the paper $\hat{\mathbf{e}}_1 = \langle 1, 0, 0\rangle$ and $\hat{\mathbf{d}} = \left\langle \frac{\sqrt{2}}{2}, \frac{\sqrt{2}}{2}, 0 \right\rangle$. On W_3, we try to maintain a null field.

Fig. 3 shows the results on W_1. The plots on the top row provide a visual comparison between the real parts of the prescribed and generated patterns. Meanwhile, the good visual match is confirmed by the plot of the pointwise relative error. It shows that the maximum relative error on W_1 is about 2.86%. The overall L^2-relative error on W_1 is around 0.004951.

Similar good results where obtained in W_2. Fig. 4(a-b) shows the prescribed and generated fields side by side. The pointwise relative error is shown in Fig. 4(c), where it can be observed that the maximum relative error is about 2.29%. Overall, the desired pattern is approximated well, with only about 0.004768 L^2-relative error.

On the far control W_3, the generated field has an L^2 norm of only about 1.06×10^{-4}. Fig. 5 shows the real part of the generated field. Note that the maximum absolute value of this field is of order 10^{-3}. The relative contrast of this field with respect to f_1 and f_2 are $C_{31} \approx 1.91394 \times 10^{-3}$ and $C_{32} \approx 1.91397 \times 10^{-3}$, respectively.

The pointwise magnitude of the density on each fictitious source is depicted in Fig. 6. It can be observed that density required to produce the prescribed fields above have values of order 10^{10} on some points in the source centered at the origin.

4.3. Planar array of sources

In the following experiment, we assume nine sources arranged in a 3×3 array in the xz-plane. Again, these sources will be modeled by spherical fictitious sources with centers at the origin, $(0, -0.03, -0.03)$, $(0, 0, -0.03)$, $(0, 0.03, -0.03)$, $(0, -0.03, 0)$, $(0, 0.03, 0)$, $(0, -0.03, 0.03)$ and $(0, 0, 0.03)$, $(0, 0.03, 0.03)$, each of radius 0.01 m. On each spherical source, we use 662 local basis functions instead of the standard 419. W_1 is a rectangular prism of dimensions $0.01 \times 0.06 \times 0.06$ centered at $(-0.04, 0, 0)$ while W_2 is a cube of side length 0.02 m centered at $(0.04, 0.02, 0)$. These near controls are discretized into 9000 points each. The far control W_3 is a sphere of radius 0.03 m centered at $(0, 0, 0.15)$. It is discretized into 5000 points. As before, we prescribe the left traveling plane wave $f_1(\mathbf{x}) = e^{i\mathbf{x}\cdot(-10\hat{\mathbf{e}}_1)}$ on W_1, the plane wave $f_2(\mathbf{x}) = e^{i\mathbf{x}\cdot(10\hat{\mathbf{d}})}$ on W_2 and a null field on W_3. A picture of the problem geometry is shown in Fig. 7.

The results of the simulation on W_1 is shown in Fig. 8. The top two plots suggest a successful synthesis of the prescribed pattern. This is confirmed by Fig. 8-(c) where it can be seen that the pointwise relative error on W_1 is at most 2.83%. The L^2-relative error on this control region is only about 5.069899×10^{-3}.

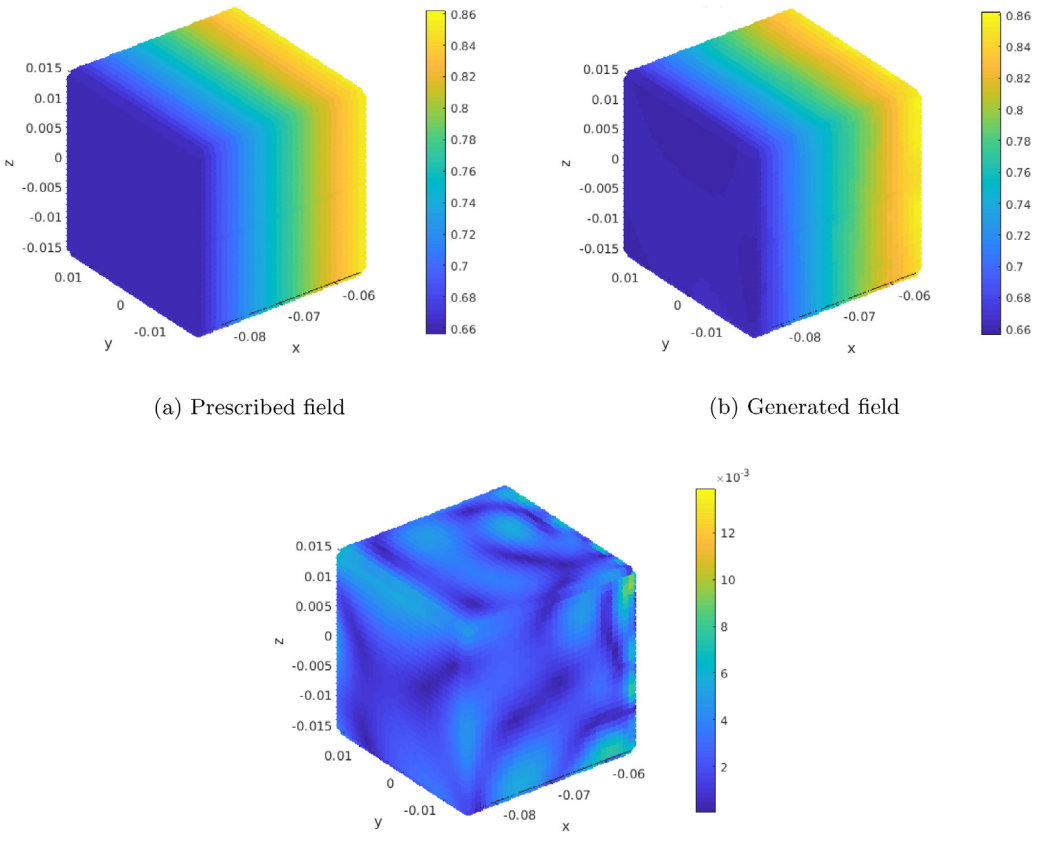

(a) Prescribed field

(b) Generated field

(c) Pointwise relative error

Fig. 13. Results of the pattern synthesis on W_1.

Fig. 9 shows how well the prescribed pattern is matched on the second near control W_2. Again, a visual comparison of the plots in Fig. 9(a)–(b) suggests a good match between the prescribed and generated fields. The third plot indicates that the pointwise relative errors are all within desirable levels with a maximum of only about 1.24%. The overall L^2-relative error is 6.012841×10^{-3}.

The real part of the generated field on the far control W_3 is shown in Fig. 10. It can be observed that the values of the field on the region are of order 10^{-3}, except for some patch where the magnitude reaches 0.0106. The L^2-norm of this field is around 7.286668×10^{-4}. The relative contrasts of this field with respect to f_1 and f_2 are $C_{31} \approx 5.876184 \times 10^{-3}$ and $C_{32} \approx 5.877013 \times 10^{-3}$, respectively.

The magnitude of the density on the fictitious sources are shown in Fig. 11. It shows that the density takes on values of order 10^9.

4.4. Nonplanar array of sources

In the following set of experiments, we consider six sources in a nonplanar arrangement and various configurations for the control regions. We use spherical fictitious sources all of radius 0.01 m with centers at points $(0.03, 0, 0)$, $(0, 0.03, 0)$, $(-0.03, 0, 0)$, $(0, -0.03, 0)$, $(0, 0, -0.03)$ and $(0, 0, -0.03)$. On each fictitious source, 419 points are chosen to be the vertices of the triangular elements.

4.4.1. Three control regions

For this simulation we consider two cubes W_1 and W_2 as near control regions, both of side length 0.03 m and discretized into 9000 points each. Their respective centers are at $(-0.07, 0, 0)$ and $(0.07, 0.02, 0)$. On W_1 we prescribe $f_1(\mathbf{x}) = e^{i\mathbf{x}\cdot(-10\hat{\mathbf{e}}_1)}$ while on W_2, we synthesize $f_2(\mathbf{x}) = e^{i\mathbf{x}\cdot(10\hat{\mathbf{d}})}$. On $W_3 = B_{0.03}(0, 0, 0.15)$ we approximate a null field. The problem geometry is sketched in Fig. 12.

The plots on the top row of Fig. 13 show the prescribed and generated fields on W_1 while the bottom plot shows the pointwise relative error. A visual comparison of the fields indicates a very good match. The pointwise relative error in the

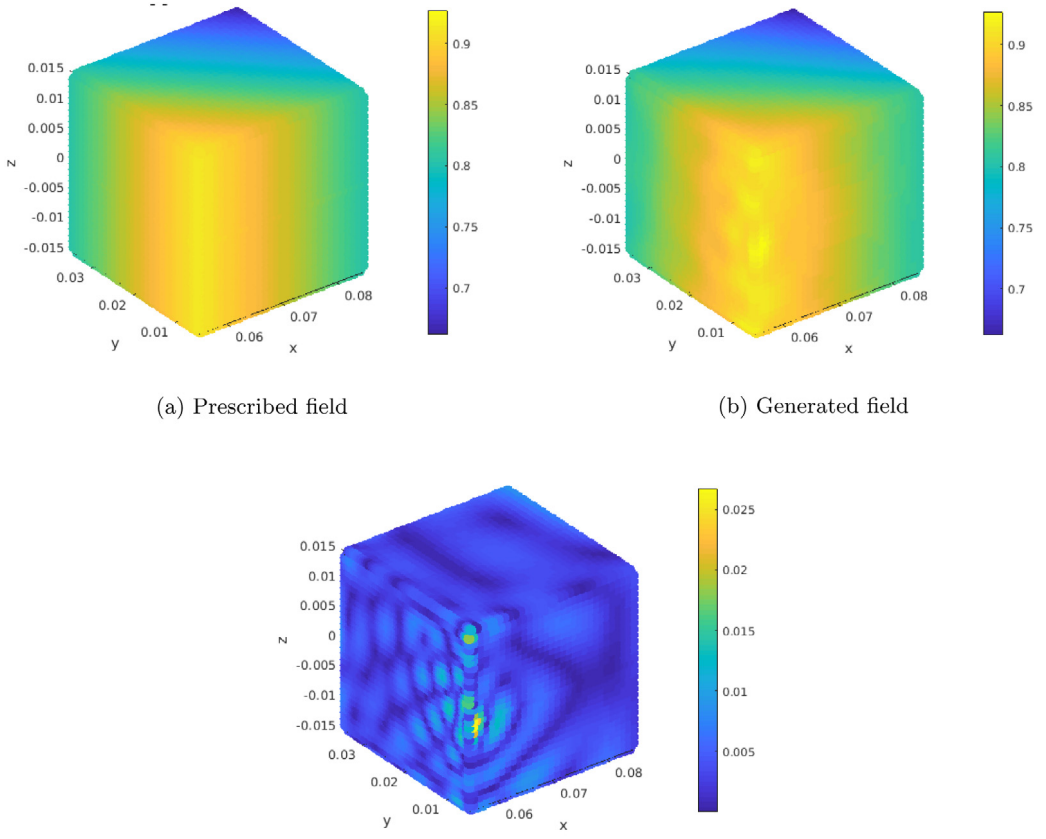

(a) Prescribed field

(b) Generated field

(c) Pointwise relative error

Fig. 14. Results of the pattern synthesis on W_2.

region is of order 10^{-3}, except on some isolated spots where it is at most 1.39%. The L^2-relative error is very low at only 3.44145×10^{-3}.

Fig. 14 shows the results of the field synthesis on W_2. The plots of the prescribed and generated fields indicate a good match. The pointwise relative error is at most 2.67%, with the higher values occurring near the frontal edge of the cube. But overall, the generated field matches the prescribed one as the L^2-relative error is just around 3.41195×10^{-3}.

A low signature was produced in the far control W_3. Fig. 15 shows that the field has absolute value of order 10^{-3} all throughout the region. The L^2 norm of the field is just around 8.9860×10^{-4}. The relative contrasts of this field with respect to f_1 and f_2 are also within desired levels, with values of just about $C_{31} \approx 7.21724 \times 10^{-3}$ and $C_{32} \approx 7.21715 \times 10^{-3}$, respectively.

The computed density on each fictitious source is plotted in Fig. 16. It shows that the there are isolated patches where the density has magnitude of around 10^{10}.

4.4.2. A near control inside the array's convex hull and an unbounded far control

In this experiment we still consider six spherical fictitious sources of radius 0.01 m in the same layout and discretization as in Section 4.4.1 but this time with a bigger separation to allow a spherical near control to fit inside the array's convex hull. The sources' centers are at $(0.05, 0, 0)$, $(0, 0.05, 0)$, $(-0.05, 0, 0)$, $(0, -0.05, 0)$, $(0, 0, -0.05)$ and $(0, 0, 0.05)$. The near control W_1 is a sphere of radius 0.02 m centered at the origin sampled into 3200 points. The far control W_2 is another sphere centered at the origin with radius 0.15 m approximated by a mesh of 3200 points. This sphere mimics the boundary of the unbounded region $\mathbb{R}^3 \setminus B_{0.15}(\mathbf{0})$. The problem geometry is pictured in Fig. 17. On W_1 we produce the plane wave $f_1(\mathbf{x}) = e^{i\mathbf{x}\cdot(10\hat{\mathbf{e}}_1)}$ and on W_2 we approximate a null field.

In Fig. 18 one can observe that the desired plane wave is approximated well with a maximum pointwise relative error of only about 0.20%. The overall L^2-relative error over W_1 is 6.458617×10^{-4}.

The real part of the field on the far control is shown in Fig. 19. The values of the field are of order 10^{-3} with a maximum of about 1.716494×10^{-3} and L^2 norm of around 3.696723×10^{-4}. The contrast between the generated fields f_1 and f_2 is $C_{21} \approx 5.834148 \times 10^{-4}$.

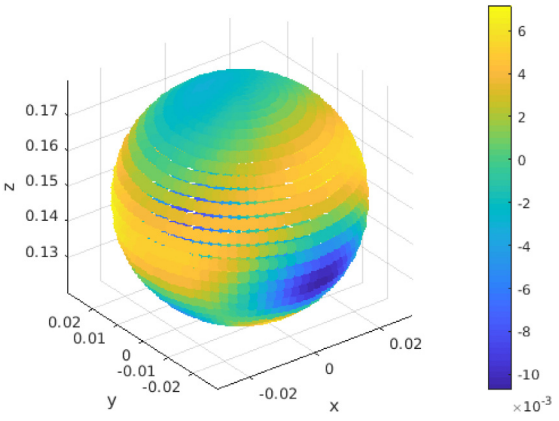

Fig. 15. Real part of the generated field on W_3.

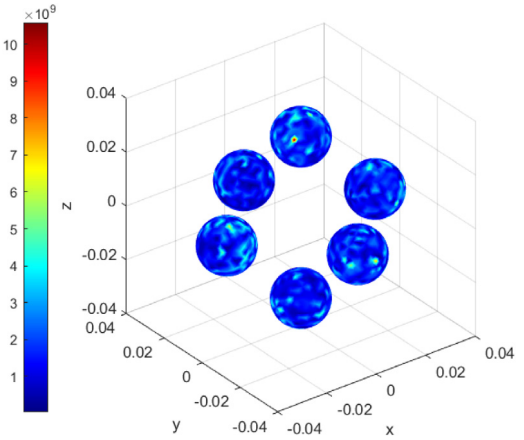

Fig. 16. Pointwise magnitude of the density w.

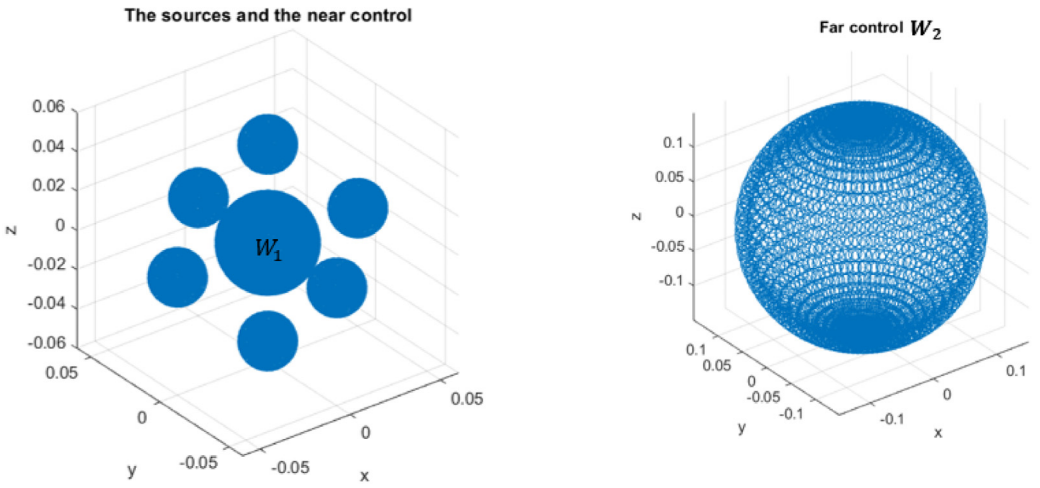

Fig. 17. Illustration of the simulation geometry.

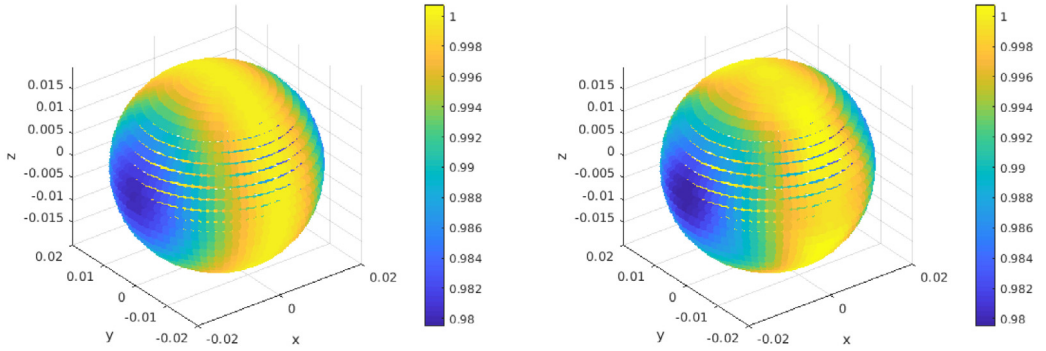

(a) Prescribed field

(b) Generated field

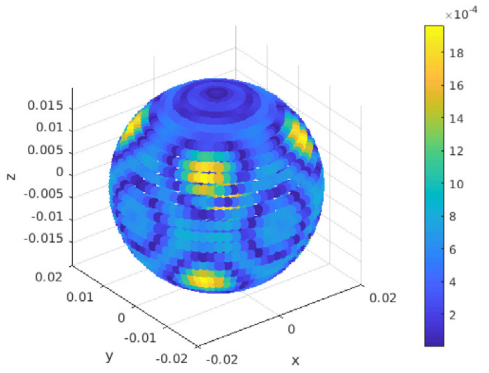

(c) Pointwise relative error

Fig. 18. Results of the pattern synthesis on W_1.

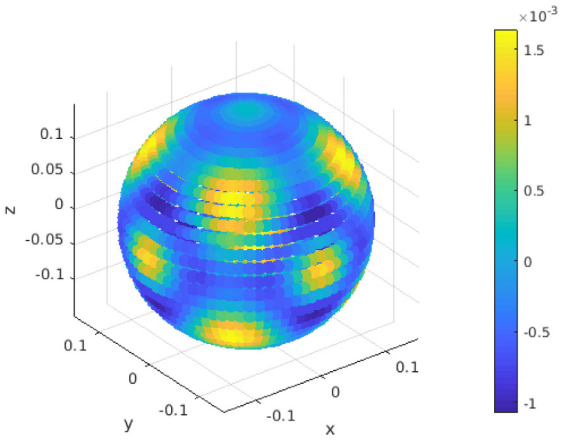

Fig. 19. Real part of the generated field on W_2.

The magnitude of the computed density on each fictitious source is plotted in Fig. 20. The maximum value of the density is less than 10^5, about 5 orders lower than the one in the previous simulation involving three control regions.

4.4.3. A near control inside the array's convex hull and a bounded far control

In this simulation, we use a similar configuration as above except that the far control W_2 is a bounded region: an annular sector $\left\{(r, \phi, \theta) : r \in [0.15, 0.2], \theta \in \left[-\frac{\pi}{4}, \frac{\pi}{4}\right], \phi \in \left[\frac{\pi}{4}, \frac{3\pi}{4}\right]\right\}$. W_2 is discretized into 9600 points. The near control

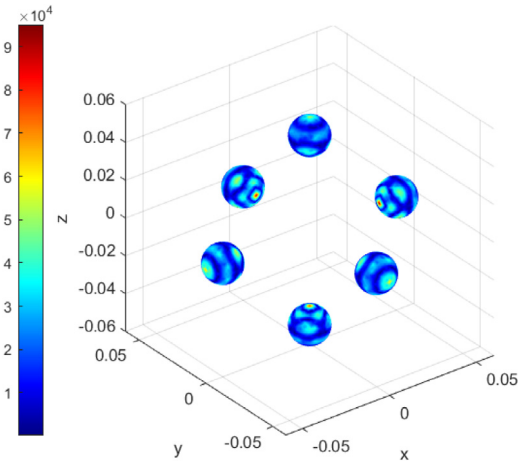

Fig. 20. Pointwise magnitude of the density w.

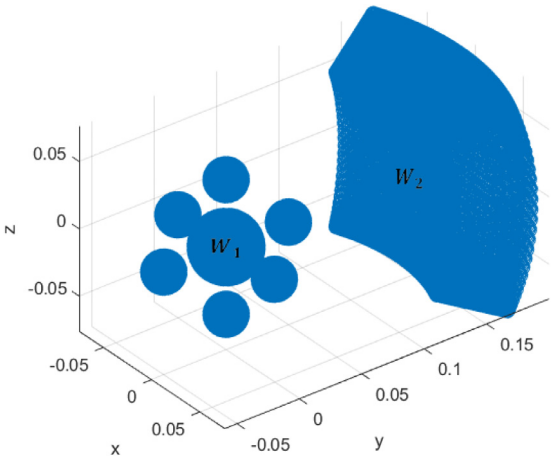

Fig. 21. Illustration of the simulation geometry.

W_1 is still the sphere $B_{0.02}(\mathbf{0})$ discretized into 3200 points. The problem geometry is sketched in Fig. 21. On W_1 we produce the plane wave $f_1(\mathbf{x}) = e^{i\mathbf{x}\cdot(10\hat{\mathbf{e}}_1)}$ and on W_2 we approximate a null field.

In Fig. 22, it can be noticed that the generated field approximates the prescribed field accurately. The pointwise relative error is at most 7.25×10^{-4} and the L^2-relative error is just about 1.904183×10^{-4}.

Fig. 23 shows a very low field signature in the far control. The field values are of order 10^{-4} all throughout the region and the field's norm is just about 1.018425×10^{-3}. The relative contrast between the fields on the two controls is also well within our desired values, $C_{21} \approx 6.344206 \times 10^{-5}$.

The magnitude of the computed density on each fictitious source is plotted on Fig. 24. It can be noted that the density is of order 10^4, the same order as in the case of an unbounded far control. However, there are more patches where high fluctuations occur and oscillations are more rampant.

4.5. A sensitivity test

In this subsection, we present a simple sensitivity test for the proposed scheme supporting the stability results in Section 3. In particular, we shall illustrate a specific case where the nonzero prescribed field is perturbed by Gaussian noise. This scenario is particularly interesting for applications such as scattering cancellation where the incoming field is measured with possible errors. Section 3 states that the relative L^2-difference between the solution obtained from the perturbed and unperturbed data will be small given that the noise level ϵ is also small.

The simulation below adopts the geometric set-up in Section 4.4.3 illustrated in Fig. 21. We still prescribed the null field on W_2 but now we impose a perturbed plane wave $f_1^\epsilon(\mathbf{x}) = e^{i\mathbf{x}\cdot(10\hat{\mathbf{e}}_1)} + \epsilon s_1(\mathbf{x})$ on W_1. Here, we fix $\epsilon = 0.01$ and take s_1 to be the standard Gaussian noise.

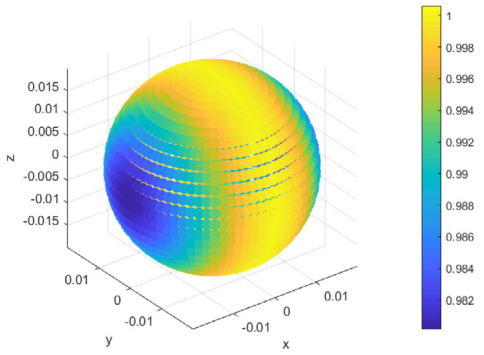

(a) Prescribed field

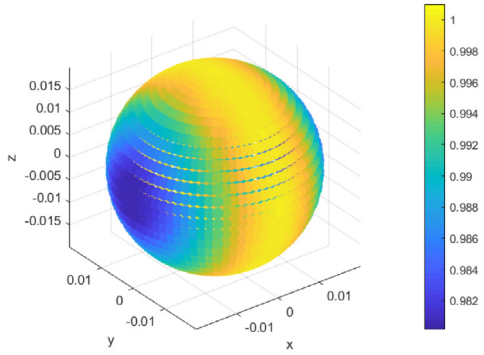

(b) Generated field

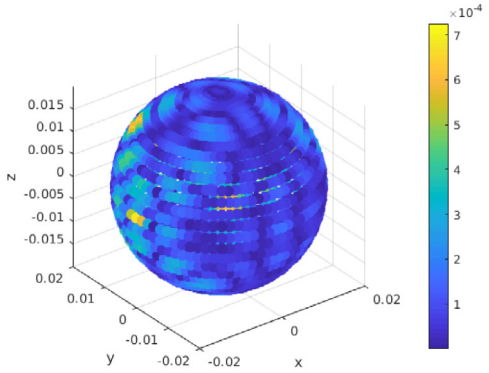

(c) Pointwise relative error

Fig. 22. Results of the pattern synthesis on W_1.

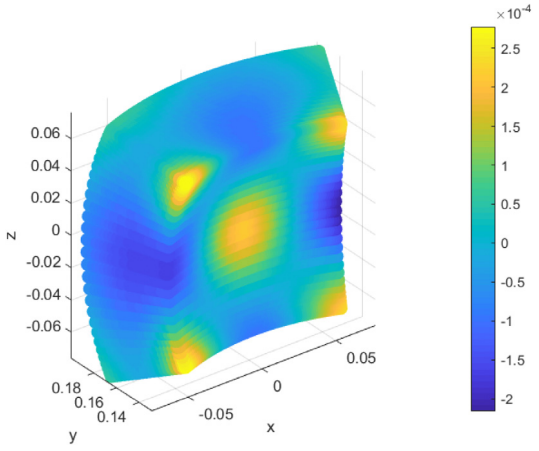

Fig. 23. Real part of the generated field on W_2.

The real part of the prescribed and generated fields, together with the pointwise relative errors are shown in Fig. 25. Again, as a further numerical stability check, the field values are plotted in a mesh of points different from the ones used in the collocation scheme. A visual comparison of the two fields shows an almost exact match. This is confirmed by the pointwise relative errors which are just at most 0.819%. Likewise, the prescribed field on W_2 is well-matched as the supremum norm of the generated field is just around 6.9×10^{-4}. Fig. 26 shows the real part of the generated field on W_2.

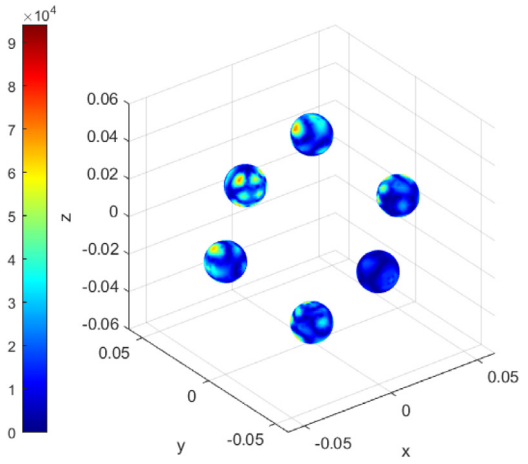

Fig. 24. Pointwise magnitude of the density w.

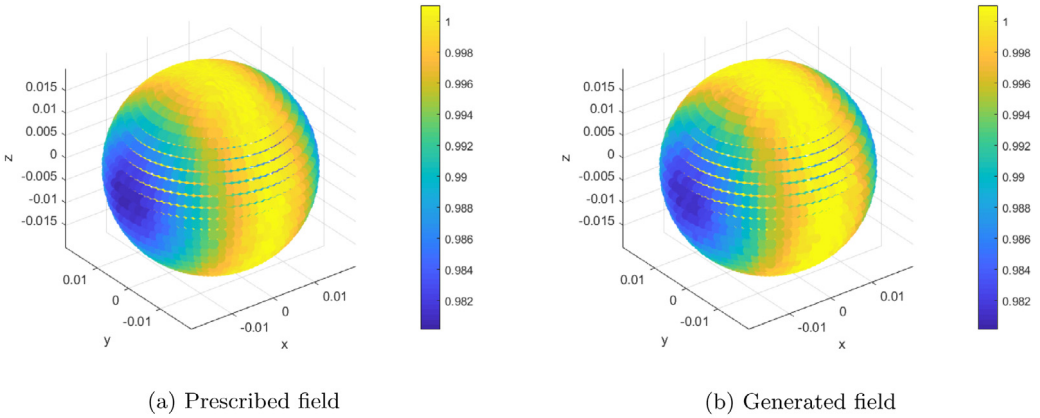

(a) Prescribed field

(b) Generated field

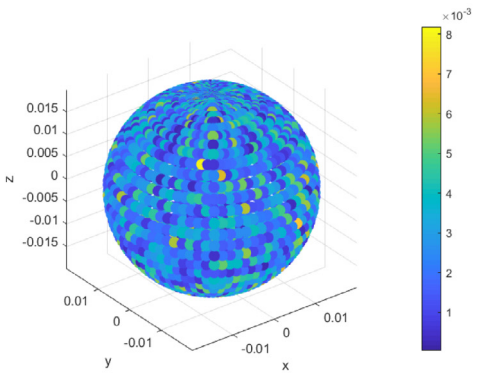

(c) Pointwise relative error

Fig. 25. Results of the pattern synthesis on W_1.

The accuracy of the field synthesis on both control regions are comparable to the ones obtained using the unperturbed prescribed field.

The computed density for the current simulation is shown in Fig. 27. The magnitude of the computed field is of the same order as that of the one for the unperturbed prescribed field shown in Fig. 24. There are also some similarities in the pattern oscillations in the density on regions across the six sources. To further verify that the numerical scheme is stable

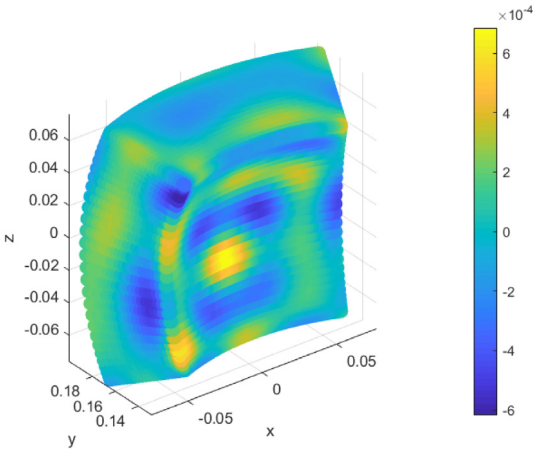

Fig. 26. Real part of the generated field on W_2.

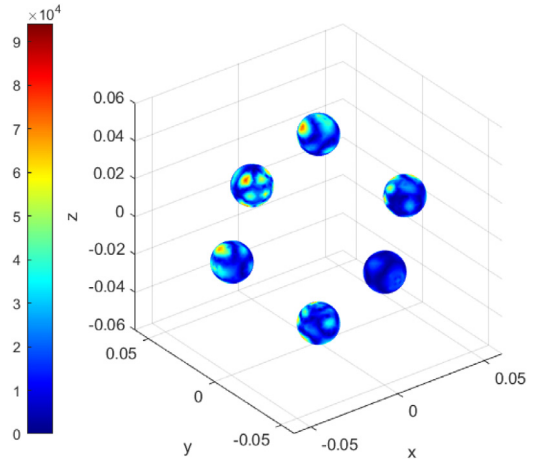

Fig. 27. Pointwise magnitude of the computed density for the perturbed prescribed field.

for this specific set-up, we compare the computed densities w^{α_0} and w^{α_ϵ} for the unperturbed and perturbed prescribed fields, respectively. The L^2-relative difference between these densities is given by

$$\frac{\|w^{\alpha_\epsilon} - w^{\alpha_0}\|_X}{\|w^{\alpha_\epsilon}\|_X} \approx 0.054338,$$

which is of the same order as ϵ. This is consistent with the results of Proposition 3.1 and is a good indication of the stability of the proposed numerical scheme against noise in the data.

5. Conclusions

In this paper we developed a functional framework and a stable numerical scheme for the active manipulation of Helmholtz fields using an array of sources. Each element in the array is a compact domain which could in practice be approximated by an array of loudspeakers thus transforming our array into an array of subarrays of loudspeakers. The propagator operator is designed to take into account the first order mutual coupling between the sources. We prove that the propagator operator has a dense range, that is, any square integrable function can be approximated by an image of a continuous function under this operator. Moreover, by extending the approach used in [30], we established that the proposed numerical scheme is stable with respect to measurement noise.

Several simulations were provided as numerical support to our theoretical results. We illustrated the possibility of finding the necessary boundary input on the sources that will accurately approximate some prescribed fields on the control regions. Though the fictitious sources used in the simulations were spheres, the use of the local basis functions in the representation of the solution allows the fictitious as well as the actual sources to assume any arbitrary shape,

as long as all the geometrical separation conditions discussed in Section 2 are satisfied (see (5) and discussion above it). The stability results were supported by a simple sensitivity test, showing that a small perturbation of the prescribed field results to a density that is relatively close to the density for unperturbed data. A detailed sensitivity analysis of this numerical scheme, to include numerical tests against measurement noise and variations in the physical parameters of the problem geometry will be included in forthcoming reports. Possible future extensions of this work include determining the optimal position of the sources with respect to some physical criterion such as the overall power required by the solution or considering the same main question but in heterogeneous environments (e.g. layered media).

Declaration of competing interest

The authors declare that they have no known competing financial interests or personal relationships that could have appeared to influence the work reported in this paper.

Acknowledgments

Daniel Onofrei and Neil Jerome A. Egarguin's works are supported by the Army Research Office, United States of America under the award W911NF-17-1-0478 while Jiefu Chen and Shubin Zeng's works are supported by the National Science Foundation, United States of America under the award numbered 1801925.

References

[1] P.A. Nelson, S.J. Elliott, Active Control of Sound, Academic London, 1992.
[2] J. Garcí a Bonito, S.J. Elliott, Active cancellation of acoustic pressure and particle velocity in the near field of a source, J. Sound Vib. 221 (1) (1999) 85–116.
[3] Jordan Cheer, Stephen J. Elliott, Multichannel control systems for the attenuation of interior road noise in vehicles, Mech. Syst. Signal Process. 60–61 (2015) 753–769.
[4] Sang-Myeong Kim, Joao A. Pereira, Antonio E. Turra, Jun-Ho Cho, Modeling and dynamic analysis of an electrical Helmholtz resonator for active control of resonant noise, J. Vib. Acoust. 139 (5) (2017).
[5] Qibo Mao, Shengquan Li, Weiwei Liu, Development of a sweeping helmholtz resonator for noise control, Appl. Acoust. 141 (2018) 348–354.
[6] Jens Ahrens, Sascha Spors, Sound field reproduction using planar and linear arrays of loudspeakers, IEEE Trans. Audio, Speech, Language Process. 18 (8) (2010) 2038–2050.
[7] Wenyu Jin, W. Bastiaan Kleijn, David Virette, Multizone soundfield reproduction using orthogonal basis expansion, in: 2013 IEEE International Conference on Acoustics, Speech and Signal Processing, 2013, pp. 311–315.
[8] Akira Omoto, Shiro Ise, Yusuke Ikeda, Kanako Ueno, Seigo Enomoto, Maori Kobayashi, Sound field reproduction and sharing system based on the boundary surface control principle, Acoust. Sci. Technol. 36 (2015) 1–11.
[9] Junqing Zhang, Wen Zhang, Thushara D. Abhayapala, Jingli Xie, Lijun Zhang, 2.5d multizone reproduction with active control of scattered sound fields, in: ICASSP 2019 - 2019 IEEE International Conference on Acoustics, Speech and Signal Processing, ICASSP, IEEE Explore (2019).
[10] Gálvez Marcos F. Simón, Menzies Dylan, Fazi Filippo Maria, Dynamic audio reproduction with linear loudspeaker arrays, J. Asian Earth Sci. 67 (4) (2019) 190–200.
[11] Neil Jerome A. Egarguin, Daniel Onofrei, Eric Platt, Sensitivity analysis for the active manipulation of helmholtz fields in 3d, Inverse Probl. Sci. Eng. (2018).
[12] Yuri Bobrovnitskii, Impedance acoustic cloaking, New J. Phys. 12 (2010) 043049.
[13] Fernando Guevara Vasquez, Graeme W. Milton, Daniel Onofrei, Exterior cloaking with active sources in two dimensional acoustics, Wave Motion 48 (2011) 515–524.
[14] Fernando Guevara Vasquez, Graeme W. Milton, Daniel Onofrei, Active exterior cloaking, Phys. Rev. Lett. 103 (2009) 073901.
[15] Fernando Guevara Vasquez, Graeme W. Milton, Daniel Onofrei, Broadband exterior cloaking, Opt. Express 17 (17) (2009) 14800–14805.
[16] Jingwei Liu, Xiaolin Wang, Ming Wu, Jun Yang, An active control strategy for the scattered sound field control of a rigid sphere, JASA 144 (EL52) (2018).
[17] Daniel Egglera, Hyuck Chung, Fabien Montiel, Jie Pan, Nicole Kessissoglou, Active noise cloaking of 2D cylindrical shells, Wave Motion 87 (2019) 106–112.
[18] Daniel Onofrei, Active manipulation of fields modeled by the Helmholtz equation, J. Integral Equations Appl. 26 (4) (2014) 553–579.
[19] Rajabi Majid, Mojahed Alireza, Active acoustic cloaking spherical shells, Acta Acust. United Ac. 104 (1) (2019) 5–12.
[20] Jordan Cheer, Active control of scattered acoustic fields: cancellation, reproduction and cloaking, J. Acoust. Soc. Am. 140 (3) (2016) 1502–1512.
[21] Stephen J. Elliot, Jordan Cheer, Jung-Woo Choi, Youngtae Kim, Robustness and regularization of personal audio systems, IEEE Trans. Audio, Speech, Language Process. 20 (7) (2012) 2123–2133.
[22] Jens Ahrens, Analytic methods of sound field synthesis, in: T-Labs Series in Telecommunications Services, Springer, 2012.
[23] D.A.B. Miller, On perfect cloaking, Opt. Express 14 (2006) 12457–12466.
[24] J. Lončarić, V.S. Ryaben'kii, S.V. Tsynkov, Active shielding and control of noise, SIAM J. Appl. Math. 62 (2) (2001) 563–596.
[25] J. Lončarić, S.V. Tsynkov, Quadratic optimization in the problems of active control of sound, Appl. Numer. Math. 52 (2005) 381–400.
[26] Zerui Han, Ming Wu, Qiaoxi Zhu, Jun Yang, Two-dimensional multizone sound field reproduction using a wave-domain method, J. Acoust. Soc. Am. 144 (2018).
[27] Zerui Han, Ming Wu, Qiaoxi Zhu, Jun Yang, Three-dimensional wave-domain acoustic contrast control using a circular loudspeaker array, J. Acoust. Soc. Am. 145 (2019).
[28] Dylan Menzies, Sound field synthesis with distributed modal constraints, Acta Acust. Acust. 98 (1) (2012) 15–27.
[29] Wen Zhang, Thushara D. Abhayapala, Terence Betlehem, Filippo Maria Fazi, Analysis and control of multi-zone sound field reproduction using modal-domain approach, J. Acoust. Soc. Am. 140 (3) (2016) 2134–2144.
[30] Mark Hubenthal, Daniel Onofrei, Sensitivity analysis for active control of the Helmholtz equation, Appl. Numer. Math. 106 (2016) 1–23.
[31] Daniel Onofrei, Eric Platt, On the synthesis of acoustic sources with controllable near fields, Wave Motion 77 (2018) 12–27.
[32] Marcus Grote, Jet Hoe Tang, On controllability methods for the Helmholtz equation, J. Comput. Appl. Math. 358 (2019).

[33] Takuma Okamoto andAtsushi Sakaguchi, Experimental validation of spatial Fourier transform-based multiple sound zone generation with a linear loudspeaker array, J. Acoust. Soc. Am. 141 (2017) 1769–1780.
[34] M.A. Poletti, F.M. Fazi, An approach to generating two zones of silence with application to personal sound systems, J. Acoust. Soc. Am. 137 (2015) 598–605.
[35] Qiaoxi Zhu, Philip Coleman, Xiaojun Qiu, Ming Wu, Jun Yang, Ian S. Burnett, Robust personal audio geometry optimization in the SVD-based modal domain, IEEE/ACM Trans. Audio, Speech, Language Process. (2018).
[36] Charlie House, Jordan Cheer, Steve Daley, On the use of virtual sensing for the real-time detection and active control of a scattered acoustic field, in: International Congress of Sound and Vibration, 2019.
[37] Li Xun, Van Manen Dirk-Jan, Robertsson Johan O.A., Curtis Andrew, Soundscape immersion using imperfect sources, in: ETH Research Collection, Phys. Rev. X (2019) (submited for publication).
[38] Darren B. Ward, Thushara D. Abhayapala, Reproduction of a plane-wave sound field using an array of loudspeakers, IEEE Trans. Speech Audio Process. 9 (6) (2001) 697–707.
[39] Aastha Gupta, Thushara D. Abhayapala, Three-dimensional sound field reproduction using multiple circular loudspeaker arrays, IEEE Trans. Speech Audio Process. 19 (5) (2011) 1149–1159.
[40] Ji-Ho Chang, Finn Jacobsen, Sound field control with a circular double-layer array of loudspeakers, J. Acoust. Soc. Am. 131 (6) (2012) 4518–4525.
[41] Bo-Hsien Wu, Gee-Pinn Too, Parameter analysis in acoustic contrast control design scheme for a loudspeaker array, J. Comput. Acoust. 20 (2012).
[42] David Colton, Rainer Kress, Inverse Acoustic and Electromagnetic Scattering Theory, third ed., Springer-Verlag, 2013.
[43] David Colton, Rainer Kress, Integral Equation Methods in Scattering Theory, in: SIAM Series: Classics in Applied Mathematics, vol. 72, 2013.
[44] Rainer Kress, Linear integral equations, second ed., Applied Mathematical Sciences, Springer New York, 1999, pp. 290–307.
[45] Milton Abramowitz, Irene A. Stegun, Handbook of Mathematical Functions with Formulas, Graphs and Mathematical Tables, 10th printing, in: Applied Mathematics Series 55, National Bureau of Standards, 1972.
[46] Mohammad Alian, Homayoon Oraizi, Electromagnetic multiple PEC object scattering using equivalence principle and addition theorem for spherical wave harmonics, IEEE Trans. Antennas and Propagation 66 (11) (2018) 6233–6243.
[47] Anastasis C. Polycarpou, Introduction to the Finite Element Method in Electromagnetics, in: Synthesis Lectures on Computational Electromagnetics, Morgan & Claypool Publishers, 2006.